Temperature profiles combined from lidar and airglow measurements

Thomas Trickl[1], Hannes Vogelmann[1], Michael Bittner[2,5], Gerald Nedoluha[3], Carsten Schmidt[2], Wolfgang Steinbrecht[4] and Sabine Wüst[2]

[1]Karlsruher Institut für Technologie, Institut für Meteorologie und Klimaforschung (IMK-IFU), Kreuzeck-bahnstr. 19, 82467 Garmisch-Partenkirchen, Germany

[2]Deutsches Zentrum für Luft und Raumfahrt (DLR), Deutsches Fernerkundungsdatenzentrum (DFD), 82234 Oberpfaffenhofen, Germany

[3]Naval Research Laboratory, 4555 Overlook Avenue, SW, Washington, D.C. 20375, U.S.A.

[4]Deutscher Wetterdienst, Meteorologisches Observatorium Hohenpeißenberg, Albin-Schwaiger-Weg 10, 82383 Hohenpeißenberg, Germany

[5]Universität Augsburg, Institut für Physik, 86159 Augsburg, Germany

Correspondence to: Dr. Thomas Trickl, thomas@trickl.de, Thomas-Knorr-Str. 47, D-82467 Garmisch-Partenkirchen, Germany; tel. +49-8821-50283; Dr. Hannes Vogelmann, hannes.vogelmann@kit.edu, Karlsruher Institut für Technologie, IMK-IFU, Kreuzeckbahnstr. 19, D-82467 Garmisch-Partenkirchen, Germany; tel.: +49-8821-258

Abstract. In this study we examine the performance of the 354.8-nm Rayleigh temperature channel of the Raman lidar at the Schneefernerhaus high-altitude research station (UFS) in the Bavarian Alps (at 2675 m a.s.l.). The temperature reference value of the retrieval is adjusted to match the temperature determined from the OH* airglow around 86 km by the GRIPS instruments at UFS. In this way the quality of the 1-h measurements of the lidar is improved above 70 km. Comparisons were made between the UFS lidar, the MLS (Microwave Limb Sounder) satellite-borne instrument and the 354.8-nm temperature channel of Hohenpeißenberg (MOHp) diffe-rential-absorption ozone lidar. Between 35 km and 70 km we see a positive offset of the UFS temperatures with respect to the MLS values of up to about 9 K. This behaviour just slightly exceeds the expectations from earlier work. Despite a horizontal distance of just 40 km between UFS and MOHp acceptable agreement below 70 km was found in several cases. However, in general, the MOHp temperatures were slightly lower than those above UFS. We discuss potential technical issues and suggest solutions for upgrading the UFS lidar system. A significant enhancement of the laser repetition rate is recommended.

Key words: Temperature, stratosphere, mesopause, lidar, MLS, OH, airglow

1. Introduction

Accurate temperature measurements at short time intervals up to the mesosphere are an important contribution to climate research and for a better understanding of the atmospheric energy balance, in particular with respect to gravity waves. This can yield information for improving atmospheric and climate models that usually only consider the comparatively small-scale gravity waves in the form of parameterizations (e.g. Kim et al., 2003; Medvedev et al., 2019). These are simplified mathematical formulations of the wave effects, as exact calculations are hardly possible for resource reasons.

In the lower atmosphere the vertical distribution of the temperature is mostly obtained from the routine radiosonde ascents that are typically carried out up to roughly 30 km twice per day. Routine measurements up to higher altitudes are to a major extent provided by satellite-based sensors yielding temperature profiles up to more

41 than 90 km (e.g., Curtis et al., 1974; Russell et al., 1999; Waters et al., 2006;). These measurements are carried

42 out with a rather dense global coverage.

43 These observations are complemented by ground-based lidar measurements. Leblanc et al. (1998) stated that

44 lidar measurements provide the best vertical resolution and accuracy for middle-atmosphere temperature studies.

45 The most commonly applied lidar method is based on Rayleigh scattering (e.g., Hauchecorne and Chanin, 1980;

46 Hauchecorne et al., 1991; Fishbein et al., 1996; von Zahn et al., 2000; Keckhut, 2004) and yields temperatures

47 typically in the mostly aerosol-free range between 30 and 85 to 95 km. The temperature inversion from Rayleigh

48 backscatter profiles is the key approach within the global Network for the Detection of Atmospheric

49 Composition Change (NDACC, https://ndacc.larc.nasa.gov). Also, daytime measurements, based on extremely

50 narrowband spectral filtering and a very small field of view, have been demonstrated (e.g., Gille et al., 1991; von

51 Zahn et al., 2000).

52 The measurements times can be excessive and must be reduced to capture the short-term temperature variability.

53 This is achieved by the use of a powerful laser and a large receiver. Sica et al. (1995) have used a 2.65-m-

54 diameter spinning liquid-mercury mirror in order to collect a maximum of 532-nm light backscattered from 12

55 W from a frequency-doubled Nd:YAG laser and, in this way, have achieved temperature measurements up to

56 more than 100 km within 6 h of lidar operation and with vertical bin sizes of 48 m. At lower altitudes, shorter

57 measurement times are possible. The propagation of tidal and gravity waves was visualized in the altitude range

58 between 33 and 50 km (Sica, 1999).

59 Traditionally, backward retrievals starting at the highest useful altitude are applied (Hauchecorne and Chanin,

60 1980). This approach converges to the correct solution within roughly 15 km. In order to obtain more

61 quantitative data also in the uppermost range forward retrievals based on optimum-estimation methods have

62 been successfully applied (Khanna et al., 2012).

63 Above 80 km fluorescence lidar methods are used both for density and temperature measurements, up to 110 km.

64 The sensitivity of laser-induced fluorescence methods is very high and has made possible single-atom detection

65 in the laboratory (e.g., Ott, 2016). In the atmosphere its application is limited to low-density conditions where

66 fluorescence quenching is avoided. Metallic species, in particular sodium, potassium and iron atoms, have been

67 successfully detected and used for temperature retrievals (e.g., Bowman et al., 1969; Blamont et al., 1972; Mégie

68 et al., 1978; Fricke and von Zahn, 1985; Granier et al., 1989; She et al., 1990; Papen et al., 1995; Arnold and

69 She, 2003; Xu et al., 2006). This method has allowed for daytime operation (e.g., Chen et al., 1996; Chu et al.,

70 2001; Höffner and Lautenbach, 2009)

71 A combination of all the three lidar methods (rotational Raman scattering (e.g., Arshinov et al., 1983; Behrendt,

72 2005; Serikov and Bobrinikov, 2009), fluorescence, and Rayleigh scattering) has been applied to generate a

73 composite temperature profile from 1 km to 105 km (Alpers et al., 2004). This approach has been extended to

74 daytime operation by narrowband spectral filtering (Gerding et al., 2010; Kopp et al., 2015; see also von Zahn et

75 al., 2000). The propagation of waves could be studied in an enormous range between 35 km and 104 km.

76 Alternatively, temperature information has been obtained from ground-based measurements of the OH* airglow

77 (e.g., Sivjee, 1992; Scheer et al., 1994; Bittner et al., 2000; 2002; Beig et al., 2003; Reisin et al., 2014; Wüst et

78 al, 2023). This method is not height resolved, but benefits from the rather confined range of the OH* airglow

79 with its peak emission height between 85 and 87 km and a full width at half maximum (FWHM) between 6 and

80 9 km on average for the Alpine region (Wüst et al., 2017). Peak emission height and FWHM show an annual and

81 a semi-annual variation due to vertical transport processes at this height. Latitudinal and longitudinal variations

82 exist to a small extent (Wüst et al., 2020). Those values are retrieved from multi-year satellite data. From

ground-based OH* airglow measurements some height information can be deduced based on the altitude-dependence of the vibrational population (e.g., Lopez-Moreno et al., 1987; von Savigny et al., 2012; Schmidt et al., 2018, Noll et al., 2023)) or from the relation between the column-integrated volume emission rate and peak emission height (e.g., Liu and Shepherd, 2006; Mulligan et al., 1995). The second method is based on the functional relationship between both parameters; this must first be determined, e.g., by adding height-resolved satellite measurements. In addition, the OH* layer has frequently been observed in limb geometry by rocket- and satellite-borne spectrometers or radiometers (e.g., Baker and Stair, 1988; Takahashi et al., 1996; Englert et al., 2010; von Savigny et al., 2013; Noll et al., 2017; Wüst et al., 2017; Li et al, 2021). Von Zahn et al. (1987), She and Lowe (1998) and Schmidt et al. (2018) compared temperature measurements of sodium lidar systems with results from OH* spectrometers. It should be noted that ground-state ($v'' = 0$) OH molecules have been observed by laser-induced ultraviolet fluorescence, i.e. in the A $^2E^+$ - X $^2II(0, 0)$ band at heights between 75-85 km (Brinksma et al., 1998). The chemiluminescent OH*-layer addressed by passive remote sensing instruments consists of pure rotational-vibrational transitions ($v'' \leq 9$) within the X ^2II electronic state and, originating from a different chemical reservoir, and peaks at higher altitudes (see Baker and Stair, 1988; Wüst et al., 2017).

In 2018 measurements of the atmospheric temperature in the stratosphere and the mesosphere were started with the 355-nm channel of the big Raman-Rayleigh lidar system at the Schneefernerhaus Alpine high-altitude station (UFS, 2675 m a.s.l.) in the Bavarian Alps (Klanner et al., 2021). These activities extend the water-vapour (Vogelmann and Trickl, 2008) and aerosol (Trickl et al., 2024) sounding at this site. The backscatter profiles, acquired within one hour, currently cover a range up to roughly 90 km. The inversion of these profiles yields temperature data up to more than 80 km if a reliable upper-end temperature reference is available. At UFS we benefit from using the temperature data from the OH* measurements at the station as a reference. This is a clear advantage with respect to comparisons with satellite data, obtained on somewhat remote orbits, or with models of unknown reliability (see Klanner et al., 2021).

In this paper, we aim at validating this new instrument, a task mandatory because of the features of the large detection system and in view of the planned archiving in the data base of the Network for the Detection of Atmospheric Composition Change (NDACC, https://www.ndacc.org). We look for the principal performance and, thus, just give comparisons with a limited number of instruments carefully characterized elsewhere (for references see below). In particular, we judge the performance by nearby lidar measurements and derive recommendations for improvements and further tests.

2. Data sources

2.1 Rayleigh backscatter measurements at 354.8 nm with a large lidar system at the Schneefernerhaus high-altitude station (Zugspitze, Germany)

Since 2009 a high-power Raman lidar system has been developed by a team from the Institute for Atmospheric Environmental Research (Garmisch-Partenkirchen, Germany; since 2009 Karlsruher Institute of Technology, IMK-IFU) that yields profiles of the water-vapour mixing ratio up to more than 20 km within one hour (Klanner et al., 2021). This lidar is located at the high-altitude station Schneefernerhaus (Umweltforschungsstation Schneefernerhaus, UFS, 47° 25′ 00″ N, 10° 58′ 46″ E, 2675 m a.s.l.) on the south side of Mt. Zugspitze (2962 m a.s.l.), about 9 km to the south-west of IMK-IFU. Because of its elevation UFS provides mostly free-tropospheric conditions (Carnuth et al., 2002). As pointed out by Trickl et al. (2024) the high base elevation yields a significant gain in backscatter signal even in the stratosphere. The system is operated side by side with a differential-absorption water-vapour lidar (DIAL; Vogelmann and Trickl, 2008; Trickl et al., 2014; 2015; 2016)

124 which allows for optimum calibration, also considering an absence of a significant bias, at least within the first

125 kilometres (Vogelmann et al., 2011; Trickl et al., 2016).

126 The Raman lidar system benefits from a large Newtonian receiver with 1.5 m diameter and a XeCl laser with up

127 to 180 W emission in single-line operation at a repetition rate of 350 Hz (Coherent, Lambda SX, with an

128 extended cavity containing an intracavity etalon and a polarizer).

129 This system can additionally yield temperature measurements by two methods. Up to the lower stratosphere the

130 temperature may be retrieved from two rotational Raman channels. This approach has been successfully tested

131 (Höveler, 2015), but has not yet entered routine operation because the focus has so far been on optimizing the

132 performance of the H_2O channel.

133 The second approach is inverting one of the two Rayleigh backscatter profiles of the lidar at 307.96 nm and

134 353.14 nm. The emission for the preferred second channel was first generated by stimulated Raman shifting the

135 output of the XeCl laser in hydrogen (Klanner, 2022). However, the performance at 353.14 nm was not reliable

136 at the high repetition rate of 300 Hz. As a consequence we added a frequency-tripled injection-seeded Nd:YAG

137 laser (Continuum, Powerlite Precision 8020) previously used in our water-vapour DIAL. This laser emits at the

138 wavelength of 354.81233 nm and yields pulse energies of 170 mJ, substantially more than the emission planned

139 from the Raman-shifted excimer laser. However, the repetition rate is limited to 20 Hz. The choice of the

140 ultraviolet wavelength provides the advantages of a larger backscatter signal than for 532.2 nm. Most

141 importantly, the light-absorption by ozone at 532.2 nm is avoided (Trickl et al., 2024).

142 A general design feature in our lidar systems is the absence of optical fibres. In this way, coupling losses, near-

143 field issues and fluorescence effects are avoided. In addition, the polarization of the transmitted radiation is

144 conserved which is essential for the chosen optical configuration of the detection polychromator (Fig. 8 of

145 Klanner et al., 2021). The 354.8-nm channel is spectrally filtered by a combination of a filter (Semrock),

146 transmitting 85 % – 90 % of the radiation between 330 and 355 nm and blocking spectral contributions outside

147 this range by at least 10^5, and a narrowband filter with a width of less than 1.2 nm (Alluxa).

148 A key issue for temperature measurements is a high quality of the detection electronics: An uncertainty of (e.g.)

149 the order of 1 K means a relative uncertainty of the measurements of less than 0.5 %. Here, we benefit from the

150 experience gained from our older systems (e.g., Trickl et al., 2020; 2023; 2024). The backscattered radiation is

151 detected with Hamamatsu R7400U-03 photomultiplier tubes (PMTs) with actively stabilized sockets from

152 Romanski sensors (RSV). In the following we describe, for simplicity, the signal voltages as positive values

153 instead of the negative ones emerging from the detectors. The performance of these detectors is highly linear for

154 peak analogues signals cautiously set to 70 mV (for 50 Ω termination) and less (Trickl et al., 2020; 2024). Here,

155 this is achieved by adjusting the laser pointing in order to maintain the maximum far-field signal level. However,

156 the analogue output is ten times more sensitive to the background signal than the PMTs from the older 5400

157 series (Trickl et al., 2020). Undershooting occurs at analogue background levels exceeding 1 mV, which does

158 not matter during night-time. However, also excessive lidar backscatter could, in principle, lead to some

159 undershooting and we have, therefore, limited the peak analogue signal even to less than the 70 mV successfully

160 applied by Trickl et al. (2020).

161 The output is registered in 12-bit transient digitizers at a range-bin size of 7.5 m (Licel). This model was

162 modified in 2010 for our ozone DIAL with a ground-free input, which was also implemented in all systems

163 digitizer systems purchased in the following. The Licel transient digitizer is optimized for very low noise (less

164 than $\pm 10^{-5}$ of the measurement range for 4096 laser shots), but, in contrast to the previously used system from

165 DSP Technology (model DSP 2020; Trickl et al., 2020), features a slight exponential wing that grows with the

166 area of the lidar backscatter signal. This wing could be easily corrected in the case of the ozone DIAL because of
167 the short decay time of the signal (Trickl et al., 2020), but is difficult to quantify for the long signal at longer
168 wavelengths. An exponential curve is subtracted, derived from a comparison with the photon-counting results at
169 high altitudes (see below). The decay constant is the same for all retrievals. An example is given in Fig. 1 (for
170 more details see Sect. 3.1).

171 Parallel to this detection channel for the analogue signal we count the individual photons in a MCS6a
172 multichannel scaler (FAST ComTec) with a pulse-pair resolution of 0.2 ns, more than sufficient for the 1.5-ns-
173 wide pulses from the detector. Because of the near-field overload of the sequential data transfer to the computer
174 we delay the start of the counting system by 10 μs. The perfect linearity of the photon-counting channels has
175 been verified by the validation of our water-vapour measurements (Klanner et al., 2021) and the performance of
176 our stratospheric aerosol measurements (Trickl et al., 2024), at least to up to 45 km. We have been optimistic
177 that the perfect linearity extends to much higher altitudes since the settling time of artefacts for this type of PMT
178 seems to be rather short. For the threshold voltage of –4 mV set at the fast discriminator (RSV) testing with
179 closed detector entrance revealed that the detection is free of "dark counts". For the temperature measurements,
180 the night-time background count rate is of the order of 0.2 counts per 7.5-ns bin and hour at the maximum
181 distance of 120 km, which allows for keeping the far-field signal-to-noise ratio as high as possible.

182 **2.2 Microwave Limb Sounder on board the Aura satellite**

183 The Microwave Limb Sounder (MLS; Waters et al., 2006) on board the Aura satellite (Schoeberl et al., 2006)
184 was launched to space in 2003. The instrument not only detects thermal emission from various molecules (most
185 recently, e.g., Nedoluha et al., 2024; 2025), but also yields vertical profiles of the atmospheric temperature up to
186 almost 100 km. 3500 vertical profiles are produced per day. The temperature retrieval is based on limb radiances
187 near the oxygen spectral lines at 118 GHz and 234 GHz. The limb-tangent pressure is derived from the shape of
188 the broadened O_2 lines.

189 Schwartz et al. (2008) analysed the quality of the temperature and geopotential height determined from the
190 measurements. Comparisons with other satellite-borne instruments indicate a negative temperature bias for
191 altitudes corresponding to pressures of 1 mbar and less. Mevedewa et al. (2014) report a negative bias of about
192 –10 K of the MLS temperature with respect to that obtained from OH measurements above 80 km.

193 For the examples shown in this paper there are just two of the 14 cases with a passage almost perfectly above
194 Garmisch-Partenkirchen during the night-time lidar observations. Given the enhanced wave activity that can be
195 expected above the Alps (e.g., Hannawald et al., 2019) this limits the quality of comparisons.

196 The geopotential height is converted to absolute height for the comparisons.

197 **2.3 GRIPS OH* chemiluminescence**

198 A closer spatial agreement with the UFS lidar is achieved with the routine OH* airglow measurements at UFS in
199 the mesopause region. The OH spectra are registered with the Ground-based Infrared P-branch Spectrometer
200 (GRIPS) instrument (Schmidt et al., 2013), integrated in the global Network for the Detection of Mesosphere
201 Change (NDMC; https://ndmc.dlr.de; e.g., Reisin et al., 2014). The centroid altitude of the airglow is 86 ± 2 km
202 and slightly varies with the season (von Zahn et al., 1987; Baker and Stair, 1988; She and Lowe, 1998; Wüst et
203 al., 2017, 2020). The aims of the research are an identification and quantification of the influence of climate
204 change, the detection of solar activity effects, the influence of atmospheric dynamics (wave activity) and the
205 validation of satellite instruments.

A survey on the relevant spectroscopic data and literature is given, e.g., by Noll et al. (2020) and Wüst et al. (2023). Wüst et al. (2023) provide a review on the recent achievements of OH* measurements. Only transitions emerging from low-lying vibrational levels appear to be suitable for sufficiently quantitative temperature derivations and we, therefore, use the low-lying (3,1) OH* transitions (Bittner et al., 2002; Noll et al., 2017). The lack of vertical resolution and the relatively large thickness of the OH* layer yields temperatures that are weighted means over a layer of the atmosphere extending over roughly 8 km.

The GRIPS instrument at UFS is oriented for slant-path detection which means that the OH* layer is reached approximately above Bozen (46.6° N, 11.0° E, Italy) south of the Central Alps, at a horizontal distance of roughly 90 km. The night-time temperature time series exhibit variations such as can be seen in the three examples shown in Fig. 1. The amplitudes of the T variations can be as high as 10 K, rarely more. In order to gain insight into the horizontal extent of these structures we, therefore, compared the GRIPS measurements with those at Oberpfaffenhofen (OPN, 48.1°N, 11.3°E, about 77 km to the north) during the same nights. The full-night average temperatures at both sites mostly agree within 1 to 3 K. The structures measured from the OPN station are not identical, but at least similar (see right panels in Fig. 2). The cases with pronounced differences demonstrate that temperature changes can occur on a confined spatial scale. This leads to uncertainties for the comparisons in Sect. 3.

The temperature in the OH* layer exhibits a pronounced seasonal dependence varying between about 170 K in summer and 220 K in winter, with average amplitudes of 17.5 K and 3.0 K of the annual and semi-annual component (see Schmidt et al., 2023). There is no consistent trend in the night-time series used this study, but a general tendency for a slight rise. Systematic temperature changes throughout the night caused by the semidiurnal migrating (12 h) tide, maximising in winter can be expected. On average this can lead to a 4-5 K temperature increase from 21 CET to 3 CET at UFS in January (compare Fig. 7 in Schmidt et al (2023)). As far as the nights used in this study show variability at all, it appears to be dominated by shorter period structures, which in some cases exhibit substantial amplitudes (Figure 2).

2.4 Temperature measurements with the Hohenpeißenberg ozone DIAL

A considerable chance for the validation of the UFS lidar is given by the routine night-time temperature measurements with the ozone differential-absorption lidar (DIAL) at the Meteorological Observatory Hohen-peißenberg (MOHp) of the German Weather Service. This station is located just 42 km to the north of UFS.

The MOHp DIAL is technically similar to the UFS lidar (Wing et al., 2021) which is an excellent basis for comparisons. For the T measurements it is also operated at 354.8 nm using a frequency-tripled Nd:YAG system (Innolas, model SpitLight 600, 120 mJ per pulse, 20 Hz repetition rate). The PMT type is similar (Hamamatsu, R9880U-110, with home-made socket) and was compared with the PMT type used at UFS without showing a difference in lidar backscatter profile. The diameter of the principal mirror of the Newtonian telescope is smaller (1.0 m), but the data acquisition is extended to full nights, which results in a high signal-to noise ratio. Exclusively photon counting is applied (FAST, P7882-2, maximum count rate 200 MHz).

The data are averaged over 150 m and, after the evaluation, smoothed to 450 m. The temperatures are routinely stored in the NDACC data base (https://ww-air.larc.nasa.gov/missions/ndacc/data.html#) from 27 km to roughly 95 km.

3. Inversion of the UFS lidar data

3.1 Temperature retrieval

The temperature profiles are retrieved from the 354.8-nm backscatter profiles as described by Klanner et al. (2021). Here, we give a few more details than in the preceding publication, based on the experience gained from the more recent measurements.

The algorithm is a modified version of the downward inversion method introduced by Hauchecorne and Chanin (1980; see also Shibata et al., 1986). This method has the advantage of self-correction within roughly 15 km from the top (reference) altitude and is less complicated than the forward inversion proposed by Khanna et al. (2012) which might be implemented at a later stage. However, we benefit from the OH* airglow measurements at UFS that allow us to shift the reference temperature to a value that yields a good match of the T profile with the OH temperature at 86 km, the average altitude of the OH* layer (Wüst et al., 2017). In cases in which the reference altitude has to be chosen below 86 km an extrapolation is estimated. In cases in which the reference altitude is above 86 km we used the temperature from the U.S. Standard Atmosphere (1976) in a first step and apply a correction in a following retrieval that shifts the temperature at 86 km to a value within the uncertainty range of the GRIPS temperature.

The main source of data is the photon-counting signal. We select a bin size of 51.2 ns, which represents a length of 7.6747 m. The PMTs were tested without input radiation and turned out to be free of background counts for 1 h of data accumulation in a single bin. Thus, no cooling of the detector is required. As mentioned, in night-time atmospheric measurements the average background count rate has been as low as roughly 0.2 counts bin^{-1} h^{-1} (Fig. 1). This is the result of careful spatial filtering and the narrow spectral filtering. This performance to a major extent excludes artefacts such as those described by Wing et al. (2018a). The backscatter profiles from the counting system are interpolated to match the 7.4948 m bin size and the vertical grid of the transient digitizer.

We start the data evaluation with visualizing the raw data and their conversion. In Fig. 1 we show an example of backscatter profiles from 9 October 2021. After determining the zero point of the distance scale we average the content of two neighbouring bins and double the size of a single data bin to 14.9896 m, which reduces the number of bins to 8000 (119.917 km). The analogue data are substantially noisier than the photon-counting data and exhibit a background drift tentatively ascribed to the performance of the transient digitizer. The 355-nm analogue profile was corrected by subtracting 3.22×10^{-4} $exp(-8.0 \times 10^{-6} \times r)$, with r being the distance above the lidar in metres. The constant of the exponential decay was used in all measurements evaluated since April 2021. This decay is 7 times slower in comparison with that in our ozone DIAL (Trickl et al., 2020) and is observable just because of the excessive operating range and the longer averaging. The fast decay component of the DIAL (277 to 313 nm) cannot be resolved because of the slower decay of the 355-nm signal, also implying the absence of absorption in ozone.

The analogue data are used from about 10 km to 30 km. As can be seen in Fig. 1 the correction is crucial for obtaining optimum temperature profiles from the analogue data for distances r up to 30 km. The data correction must be made with care because of the enormous requirements for the temperature measurements. Below 10 km the signal is partially cut off by one side (blade) of the entrance aperture, the laser beam being adjusted to limit the near-field peak signal. Above 30 km the photon-counting signal is taken where it is fully linear. No dead-time correction has been implemented in this channel as frequently done in lidar systems based on counting alone. All backscatter signals are carefully compared with simulations from meteorological data (see also below).

287 The analogue measurement in Fig. 1 is the best in comparison with those in the other measurements obtained
288 since spring 2021. In other cases, slight deviations from the clean exponential behaviour were observed that we
289 tend to ascribe to interference of the magnetic field of the laser flashlamps as found in earlier work (e.g., Trickl ,
290 2010). The use of a diode-laser-pumped laser system is planned (see Sect. 4). For such a laser system we have
291 not found any similar interference (Trickl et al., 2024).

292 For reducing the data noise we apply altitude-depended smoothing with a numerical filter as described by Trickl
293 et al. (2020). The bin interval of the Blackman-type filter is nonlinearly enhanced using the formula

294 $$a + i^2 \times b$$

295 at bin i (size 14.9896 m), with normally a = 20 and b = 4×10^{-5}. This results in a variation of the VDI (1999)
296 vertical resolution from 58 m at the ground to 1216 m at 50 km and a maximum of 2908 m at and above 76.7 km
297 a.s.l. (Trickl et al., 2020; VDI, 1999; see (Iarlori et al., 2015; Leblanc et al., 2016) for other definitions). The
298 VDI resolution is defined as the range difference between 25 % and 75 % of the response to a Heaviside step.
299 Above this, the vertical resolution stays constant to limit the computation requirement.

300 As described by Klanner et al. (2021) we first calculate the atmospheric density in a fully quantitative Klett-type
301 approach with downward integration from the far end (Klett, 1981; 1985):

302
$$n(r) = \frac{n(r_{ref})\ r_{ref}^2 S(r_{ref})}{r^2 S(r) + 2n(r_{ref})\sigma_R \left[\int_r^{r_{ref}} r'^2 S(r')dr'\right]} \ , \tag{1}$$

303 S(r) being the backscatter signal, r_{ref} the reference distance and σ_R the Rayleigh extinction coefficient. Here, the
304 misprint in Eq. 1 of Klanner et al. (2021) is corrected that has not been part of the computer program. The far-
305 end reference density $n(r_{ref})$ is varied for matching the density derived from the Munich radiosonde (launched at
306 Oberschleißheim, station 10868, about 100 km roughly to the north), also making comparisons with the densities
307 from NCEP (National Centers for Environment Prediction) at higher altitudes. We download the sonde data from
308 https://weather.uwyo.edu/ upperair/sounding.html. The NCEP altitudes, pressures and temperatures are taken
309 from the web site of the Network for the Detection of Atmospheric Composition change as calculated for
310 Garmisch-Partenkirchen (https://www-air.larc.nasa.gov/ missions/ndacc/data.html?NCEP=ncep-list). The NCEP
311 listings are available up to roughly 55 km.

312 From the density n we obtain the temperature profile by applying

313
$$T(z) = T(z_0)\frac{n(z_0)}{n(z)} + \frac{m_{air}}{k\ n(z)}\int_z^{z_0} n(z')g(z')dz' \ , \tag{2}$$

314 with z being the altitude above sea level, z_0 the far-end reference altitude, m_{air} = 28.9644 u (U.S. Standard
315 Atmosphere, 1976; 1 u = $1.66053904 \times 10^{-27}$ kg (Mohr et al., 2016)) the mass of an "average air molecule", and g
316 the gravitational acceleration,

317
$$g(z) = g_0 \left(\frac{r_E}{r_E + z}\right)^2 \ ,$$

318 with g_0 = 9.80665 m s^{-1} and the earth radius r_E = 6356766 m (U.S. Standard Atmosphere, 1976). In the U.S.
319 Standard Atmosphere the atmosphere is regarded as well mixed up to 86 km, which suggests to be cautious at
320 the highest altitudes accessible.

321 The inversion starts at the highest reasonable altitude, mostly below the upper end of the density profile.

322 Normally, we take the temperature for the start altitude from the U.S. Standard Atmosphere (1976) as the

323 reference. The algorithm in Eq. 2 is self-correcting: Within 15 km of downward integration the temperature is

324 does no longer vary as a function of the reference value by more than ±2 K (Klanner et al., 2021), as a

325 consequence of the density dependence of the first term of Eq. 2. It turned out that the influence of the reference

326 density (Eq. 1) is very low and can be neglected for the careful adjustment made (see above).

327 In eight of the fourteen cases examined we had to make adjustments of the reference temperatures to match the

328 temperature of the GRIPS instrument at 86 km, or, in one case without GRIPS measurements, the range of MLS

329 values. For a perfect comparison of lidar and GRIPS an extension of the operating range of the lidar to more than

330 100 km is desirable. Wing et al. (2018a) recommended to use the MSIS model output as a reference. The result

331 was not satisfactory at all (Klanner et al., 2021) and we decided to use the GRIPS temperatures.

332 The retrieval of temperature from lidar data is a highly demanding task. For instance, an uncertainty of 1 K

333 means a relative uncertainty of 0.33 % at a temperature of 300 K. Thus, a very high quality of the backscatter

334 signals is a prerequisite for reasonable results.

335 Aerosol corrections have been tested and lift the temperature in a range around 22 km, typically by 2 to 4 K

336 under the conditions of the cases chosen. The aerosol backscatter coefficients are taken from the stratospheric

337 aerosol measurements (Trickl et al., 2024) from adjacent days and converted from 532.24 nm to 354.8 nm by

338 multiplication with 1.992 (Jäger and Deshler, 2002; 2003). However, such an effort makes sense just if the

339 quality of the exponentially corrected analogue signal matches that in Fig. 1 which was the case just for two

340 measurements (16 November 2018 and 9 October 2021). In the other cases, the analogue signal background

341 exhibited slight modulations perhaps caused by the magnetic field of the flashlamp-pumped laser. Here, the

342 exponential correction is adjusted to generate temperature values matching those from the midnight Munich

343 radiosonde (station 10868).

344 **3.2 Uncertainties**

345 As pointed out in the U.S. Standard Atmosphere (1976) the atmospheric composition is homogeneous mixed up

346 to 86 km. Local short-term perturbations are averaged away by the long signal acquisition time of 1 h.

347 The uncertainty from shot noise, as derived from the smoothed signal, is of the order of 10 K at 70 km. We use a

348 scaling law

349
$$u = \sqrt{u_0^2 + (u_1 \frac{r^2}{r_{ref}^2})^2 + (u_2 S(r))^2} \ , \tag{3}$$

350 for the uncertainties, with coefficients u_0, u_1, and u_2 that are estimated by comparison with reference

351 measurements at lower altitudes and the shot noise at higher altitude. The second term in Eq. 3, quadratic in r,

352 reflects the quadratic rise of the noise of the unsmoothed quantities. We select the reference distance r_{ref} at the

353 upper end of the data evaluation range. By the approach with Eq. 3 considerable computation efforts have been

354 avoided. The results of Sect. 4 verify the approximation.

355

356

357

4. Results

4.1 UFS lidar results

The lidar test phase presented in Sects. 4.1 to 4.3 covers the 14 measurements made between November 2018 and February 2022. In addition, four separate night-time series are presented in Sect. 4.4.

In Fig. 3 we show the result of a revised data evaluation of the example shown by Klanner et al. (2021) based on the slightly enhanced smoothing described in Sect. 3.1 and an exponential correction of the analogue profile that was missing in the earlier evaluation. In addition, an aerosol correction was made that resulted in good agreement with the temperature profile of the Munich radiosonde down to 12 km. The ripple below 32 km is a result of the aerosol correction. Below 12 km the signal was partly cut off by rotating the laser beam to shift the return bundle towards one side the entrance aperture of the detection system in order to limit the maximum signal.

The GRIPS value was determined from an average of the GRIPS temperatures during the measurement period of the lidar, which was done for all cases. The error bar represents the standard deviation for that period and does not include the uncertainty due the missing co-location caused by the slant-path OH* measurements (see Sect. 2.3). This influences the results in an uncertainty of ±5 K, sometimes more. The GRIPS value in this example agreed sufficiently well with the lidar temperature generated by initiating the retrieval with the U.S. Standard temperature at 88 km. Thus, the calibration was not shifted.

The NCEP data agree well with the radiosonde temperatures up to the operating range of the balloon. There is a small deviation with respect to the lidar at 40 and 46 km. We do not know if this bias is caused by a vertical shift of the NCEP profile.

We also added temperature profiles from MLS and the MOHp lidar. Unfortunately, no T profile from MOHp was available for the same night, and we took the results from the two neighbouring measurement nights. The average of both MOHp profiles agrees quite well with the UFS profile to about 70 km. The MLS profiles are shown for about 13:31 CET (Central European Time, three thin orange lines) and about 3:05 CET on 17 November 2018 (three blue lines), named "noon" and "midnight", respectively. The agreement should be better for the "midnight" measurement, but the best agreement is limited to the spike region around 64 km. In principle, this could be ascribed to the pronounced difference in longitude.

4.1 Comparisons of the temperatures from the UFS lidar and the NCEP archive

Up to the burst altitudes of the balloons (mostly 30 to 33 km) the temperature of the Munich radiosonde is nicely reproduced (see examples: Fig. 3 and Sects. 4.2, 4.3). For higher altitudes the temperatures are compared for all NDACC stations from the NCEP data. The NCEP profiles are listed up to roughly 55 km. Again, geopotential heights are converted to absolute heights.

Trickl et al. (2024) found for the evaluation of stratospheric aerosol that the Rayleigh reference profiles calculated from the NCEP density and temperature data look highly reliable up to the chosen Klett (1983) reference distance of 45 km (absolute altitude 47.675 km). However, the requirements for the temperature are much higher. For the temperature data we found, in comparison with the UFS lidar, reasonable agreement up to 35 km, but sometimes deviations above this altitude (and below 50 km) of up to about 10 K occur (see Fig. 3 and examples in the following sections; in one case even more). Sometimes there is the impression of a vertical shift

396 of the NCEP profile or a slightly wrong gradient in the range of the strongest temperature increase. The NCEP
397 profiles are calculated for noon UTC (13:00 CET) which certainly limits the comparability.

398 **4.2 Comparison the temperatures from the UFS lidar and MLS**

399 After initially concentrating just on the co-ordinates of the satellite for a given date (e.g., Klanner et al., 2021)
400 we now also looked at the times of the MLS overpasses, which resulted in a somewhat different view. The mean
401 passage times specified were 1.38 (±0.40) h with respect to noon (CET) and 2.69 (±0.39) h with respect to the
402 following midnight (CET). The "midnight" passages can be expected to be the better choice for the comparisons
403 with the early-night lidar measurements and were normally taken for the statistical evaluation. Morning times on
404 a given day were no longer used. For the downloaded data we consistently found the three latitudes 45.9º N,
405 47.35º N and 48.8º N which is sufficiently close to UFS (within ±1.6º). By contrast, the longitudes were not
406 reproducible and ranged between 3.2º E and 20.7º E. For just two of the days the longitude perfectly matched
407 that of UFS. However, these profiles did not agree with those from the lidar significantly better. In two cases one
408 measurement time group of MLS was missing, and we took the profile for a passage at a time difference of about
409 ±12 h with respect to midnight.
410 In addition to Fig. 3 we show in Fig. 4 six examples of comparisons. On average the positive bias of the
411 temperatures from the lidar and that from MLS remained. The best agreement below 70 km is seen in the
412 midnight comparisons (MLS: thin blue lines) in Fig. 3 and Fig. 4e. In three of the cases (not shown in Fig. 4) big
413 positive temperature peaks exceeding the estimated uncertainties could be seen above 70 km in the lidar data.
414 One of these cases is shown in Sect. 4.3. In addition, in Fig. 4f there is a rather excessive deviation between lidar
415 and MLS at 69 km, but here the temperature difference with respect to the MOHp lidar is smaller (thick blue
416 line). Because of the good latitudinal matching this discrepancy is strange. We are unable to explain it. One
417 could think either about wave effects or about an outlier of the lidar measurement. For identifying waves one
418 needs time series which is possible because of the one-hour time resolution of the system.
419 A very strange deviation was untypically found at rather low altitude for 12 December 2018 (not shown). At the
420 moderate altitude of 46 km the midnight MLS temperature was lower by as much as 25 K than that from the
421 lidar. The difference with respect to the MLS noon temperatures had been just 15 K, also this, however, being
422 out of any expectation for this altitude range. Below 35 km and above 57 km the agreement was reasonable to
423 excellent. For our statistical analysis (see below) we took the noon profile.
424 In Fig. 5 we show the differences of the profiles for all measurements, as well as the arithmetic average and the
425 positive and negative standard deviation. For the averages we selected the MLS latitude 47.35º N, −0.07º away
426 from that of UFS. In all but two cases the "midnight" MLS profile was taken. The maximum deviations for the
427 lidar are 9.4 K at 52.8 km and 8.6 K at 68.6 km. The minimum difference is found at 61.0 km is 3.1 K. In three
428 profiles the data in a short altitude range below 70 km with excessive deviations were excluded from the
429 averaging.
430 The negative temperature deviation of MLS confirms the findings in earlier work. Schwartz et al. (2008)
431 compared the MLS temperature profiles with those from several other satellite-borne sensors. They abruptly
432 started to depart from the other profiles above 45 km, the maximum negative offset reaching values between 5
433 and 8 K. The minimum difference around 60 km is also confirmed. Wing et al. (2018b; 2021) found a similar
434 behaviour for other Rayleigh lidar systems.
435

4.3 Comparisons of the temperatures from the UFS and MOHp lidar systems

Instead of comparing the UFS results with another satellite-borne sensor such as the proven SABER (Sounding of the Atmosphere using Broadband Emission Radiometry; launch: December 2001; Russell et al., 1999; Mertens et al., 2009; Esplin et al., 2023) we preferred to compare our temperature results with those of the nearby MOHp ozone lidar. The advantage is the mentioned relatively small distance between the two lidar sites The MOHp temperatures have been demonstrated to match the SABER temperatures almost perfectly (Fig. 10 of Wing et al., 2021), as is the case also for other lidar stations (e.g., Cooper, 2004; Wing et al., 2018b; Dawkins et al., 2018). Thus, we see the MOHp lidar as a suitable reference (see also Steinbrecht et al., 2025). During 9 of the 14 measurement nights at UFS the MOHp lidar was operated as well. The MOHp temperature are archived above 27 km.

As expected from earlier work (e.g., Wing et al., 2018b; 2021) the UFS and MOHp lidar temperature channels yield a better agreement than the comparisons of the UFS lidar with MLS. However, the temperatures for the two lidar sites may differ. In Fig. 6 the best case is presented with almost identical values up to 71 km (8 November 2021). Above this altitude the UFS temperature profile exhibits a pronounced peak strongly outside the estimated uncertainty above this altitude. The MLS values sometimes deviate strongly which is associated with bad temporal and spatial co-incidence.

The excellent agreement of the lidar results at both stations in Fig. 6 suggests that there is no fundamental mismatch of the retrieval algorithms. Also in Fig. 7 the results do not differ much, except for the range above 66 km. There, the deviation is, still, within the expected uncertainty or the temperature variations suggested by the variability in the GRIPS data. This agreement also suggests the absence of fluorescence effects of the interference filters or PMT issues (see Sect. 5).

However, the examples in Fig. 4 demonstrate that there is, on average, a systematically lower temperature in the MOHp values. This is somewhat surprising because of the good matching of the MOHp temperatures with SABER (Wing et al., 2021) and a similar average offset between SABER and MLS (Schwartz et al., 2008) as found for the UFS lidar in Fig. 5.

At least, the agreement between the two lidar systems is better than that in Fig. 5. This is shown in summary in Fig. 8, prepared in the same way as Fig. 5. The average temperature differences between UFS and MOHp are positive up to almost 80 km, even at the lowest altitudes, where the UFS values agree mostly well with the sonde data (as visible in the examples also down to below 20 km).

This behaviour will be discussed in Sect. 5.

4.4 Comparisons of night-time series at UFS with the MOHp all-night temperature profiles

One issue of comparisons of the lidar measurements at UFS and MOHp is that the measurements at UFS are confined to one hour and were, until 2022, concentrated to the first half of the night, whereas the soundings at MOHP cover full nights. Although on average a night-time temperature increase has been found at the altitude of the OH layer and ascribed to atmospheric tides we speculated on potential night-time cooling of the atmosphere below. Of course, such an effect is difficult to evaluate in the presence of pronounced atmospheric wave activities.

We, therefore, carried out four night-time series in November 2024, i.e., after the end of the period of investigation in the previous sections (February 2022). The measurements were carried out at half-hour intervals with durations of just half an hour, which resulted in a higher variability of the values at high altitudes than for the 1-h measurements. Figure 9 shows the examples for the last two of the four nights, for which MOHp

477   reference profiles existed and for which the GRIPS temperature variability was low. During these nights the

478   differences of the single-night average UFS and the MOHp temperatures are rather small. Very few profiles

479   depart strongly from the average, beyond our expectations.

480   In Fig. 10 we present temperature time series of these two nights for altitudes differing by 5 km between 30 and

481   80 km. Up to 55 km the series are sufficiently smooth to allow us to judge temperature trends. There is no

482   indication of major night-time atmospheric cooling over a large altitude range, which is favourable for a good

483   agreement of the two lidar systems. The negative temperature development at 45 km and 50 km during the night

484   between 4 and 5 November could be an exception, but does not exceed the range of the temperature variability.

485   For the other two nights no cooling outside the temperature variability is observed (not shown).

486   Due to the enhanced noise of the half-hour sounding many lidar temperature profiles could not be evaluated to

487   clearly beyond 80 km. This made the calibration by using the GRIPS values impossible. Nevertheless, we used

488   estimates of the behaviour in the uppermost part of the measurements for a reasonable approach, also looking at

489   the MOHp profiles. Thus, the results above 70 km are somewhat influenced by the reference to GRIPS. As a

490   result of this and because of the smaller number of cases that can be averaged at the highest altitudes the

491   standard deviation diminishes beyond 80 km.

492   **5. Discussion and Conclusions**

493   Klanner et al. (2021) demonstrated that with a powerful XeCl laser and the large receiver Raman backscatter

494   signal accumulated within one hour from atmospheric water can be resolved to more than 25 km during night-

495   time, allowing us to retrieve useful H_2O mixing ratios to at least 20 km. In this study we examine the

496   performance of the Rayleigh temperature channel also for one-hour measurements.

497   The smoothed backscatter signals of the temperature channel can be discerned from the background up to more

498   than 90 km. Since this corresponds to a small fraction of one count per bin the smoothing must be strong and

499   currently limits the vertical resolution at high altitudes to 2.9 km (as defined in the 1999 VDI guideline). The

500   temperatures can be retrieved starting at several kilometres below this. The retrieval in the uppermost part of the

501   altitude range benefits from the simultaneous OH* measurements at UFS. In cases when the useful range of the

502   lidar ends below 86 km estimates from extrapolations are used.

503   The rather systematic positive offset of the lidar temperatures with respect to those from MLS between roughly

504   40 km and 70 km confirms the expectations from earlier work (Schwartz et al., 2008; Medvedeva et al., 2014;

505   Wing et al., 2018b; 2021). As mentioned, other satellite-borne sensors, in particular SABER, have shown an

506   excellent agreement with lidar temperature data above several stations including MOHp.

507   The agreement of the UFS lidar with the "off" wavelength channel of the MOHp DIAL is better, but on average

508   the UFS temperatures from roughly 45 km to 70 km also deviate positively. However, several profiles agree

509   really well which, together with the agreement below 45 km, suggests that there is no fundamental problem with

510   the retrieval algorithm.

511   A positive temperature offset means a smaller slope of the air density and, thus, slower decay of the lidar

512   backscatter signal. A slower decay of the backscatter signal would be typical of known technical artefacts that

513   will be discussed below. Since the UFS temperatures are higher than those of MOHp this could suggest that the

514   problems are more on the side of the UFS lidar.

515   Signal components exhibiting exponential decay are typical artefacts in lidar signal processing. For example,

516   slow fluorescence decay of optical components, in particular of interference filters, could yield slightly higher

517   temperatures above a certain threshold altitude. A threshold behaviour around an altitude of about 40 km is,

518 indeed, observed. However, because of the excellent agreement between the two lidar systems in several cases

519 we hesitate to assume the presence of fluorescence.

520 In addition, electronic artefacts must be considered. Wing et al. (2018a) attribute positive T biases above 70 km

521 to some extent to electronic cross talk or bursts of transient electronic signals and present a method to discard

522 bad profiles influenced by a shot-by-shot numerical analysis. Such an approach is helpful, but limited to low to

523 moderate laser repetition rates because of limits in computation speed. In any case, due to sufficient spatial

524 filtering in our receiver our far-field background count rate is of the order of 0.2 h^{-1} bin^{-1} which means

525 negligible interference of bursts. In fact, PMT testing with covered photocathode in the detection system verified

526 even the mostly complete absence of dark counts. The detection system is located far away from sources of

527 electromagnetic interference in a metallic tower outside the building.

528 Small exponential wings of the backscatter signal that could give rise to higher temperatures can be caused by

529 signal-induced nonlinearities of photomultiplier tubes (Bristow et al., 1996). Two effects must be considered,

530 signal-induced gain change due to overload of the final dynode stages and signal-induced emission of the

531 photocathode. The first type is avoided by limiting the signal, the second one seems to be suppressed in the PMT

532 model chosen to a high degree by kinetic-energy filtering (removal) of the artificial low-energy electrons.

533 Indeed, signal-induced nonlinearities have been found to be absent for the Hamamatsu R7400 detectors under

534 conservative operating conditions, in particular for photon counting (e.g., Trickl et al., 2020; 2024). Kreipl

535 (2006) determined the 1/e decay time of an overloaded R7400-03 cathode to less than 30 µs, i.e., much shorter

536 than the decay time of the backscatter signal of our temperature measurements. These tests had been carried out

537 at a cathode illumination higher by almost two orders of magnitude. In summary, we can exclude signal-induced

538 nonlinearities as the reason of the positive temperature deviations.

539 There is one important difference between the lidar measurements at UFS and MOHp. The measurements at

540 UFS have taken place before midnight or around midnight the latest. At MOHp, with the exception of the

541 favourable case in Fig. 6, the data acquisition lasted all night, with measurements times up to more than 12 h

542 during the cold season. Atmospheric cooling during the second part of the night could serve as an explanation

543 the observed difference. The GRIPS measurements examined in this study do not reveal reproducible cooling in

544 the mesopause region with progressing night. The GRIPS temperatures tend to grow with time. At lower

545 altitudes (e.g.) the examples of Kopp et al. (2015) do not allow us to resolve a temperature change because of the

546 wave structure superimposed on the temperature profiles. At least our night-time measurement series in

547 November 2024 demonstrate in these cases that in the almost complete absence of atmospheric cooling the

548 temperature differences obtained at UFS and MOHp stay strongly below the variability of the 0.5-h UFS lidar

549 data.

550 A bias caused by misalignment can be excluded since this would lead to deviations at low altitudes. This kind of

551 problem has been limited to altitudes below 20 km.

552 Apart from these issues a range extension to more than 105 km is desirable since this would allow us to retrieve

553 temperatures with uncertainties of the order of ±5 K up to almost 90 km, which covers the well-mixed part of the

554 atmosphere (U.S. Standard Atmosphere, 1976). The GRIPS measurement range would then be included in the

555 useful operating range of the lidar and the temperature obtained from the spectra could be controlled by vertical

556 sounding. As one can judge from Fig. 1 such a range extension would require a ten times higher laser power.

557 Since the pulse energy of the current laser is adequate for not exceeding signal levels that ensure linear detection

558 a much higher pulse repetition rate would be the solution. Diode-laser-pumped Nd:YAG with similar third-

559 harmonic pulse energies but a repetition rate of more than 300 Hz are meanwhile commercially available. 300

Hz would match the repetition rate of the XeCl laser and water vapour and temperature measurements could be made simultaneously, with delayed pulses in order to minimize spectral interference. This would mean 15 times the power of the current transmitter.

In three cases we observed excessive temperature peaks around and above 70 km. Because of the low signal level at these altitudes we cannot exclude signal outliers which, again, calls for a higher backscatter signal. However, temperature excursions of the order of 20 K in the mesopause region have been presented in earlier work and attributed to waves (e.g., Kopp et al., 2015). A clear identification of gravity waves requires to carry out our time series with a better signal-to-noise ratio.

In addition, an influence of particles or fluorescence from meteorites must be distinguished. One example of a potential particle layer observed at 54 km with our stratospheric aerosol lidar (Trickl et al., 2013; 2024) is given in Fig. 11. An identification of the presence of particles cannot be achieved with a simple backscatter lidar. The particle contribution can be removed by spectral filtering the scattered light from a narrowband frequency-doubled Nd:YAG laser in iodine (Piironen and Eloranta et al., 1994) . For our system we could think of additional measurements at the also available 532.2-nm laser emission with an iodine filter as successfully implemented in our mobile aerosol lidar before (Giehl and Trickl, 2010; Wandinger et al., 2016). The problem of the light absorption in ozone at 532.2 nm does not matter at high altitudes.

The advantage of symbiotic use of the GRIPS observations at UFS could be strengthened by adding a vertically pointing spectrometer. In the near future, the current set-up with two identical spectrometers will be extended by a third spectrometer that will be aligned for parallel measurements with the laser beam. This, together with less noisy lidar data, would simplify the interpretation of remaining differences. More detailed studies of the airglow layer could be made by tuning the fundamental wavelength of the Raman lidar wavelength to 308.15 nm where OH laser-induced fluorescence can be excited (Brinksma et al., 1998).

After the completion of the upgrading the beginning of routine lidar measurements is planned, as a potential contribution to NDACC.

5 Data availability

Lidar data from the UFS lidar can be obtained from the authors, but are currently flagged as preliminary. GRIPS temperatures are available at https://zenodo.org/records/15267440. MLS v5 temperature data are available at https://disc.gsfc.nasa.gov/datasets?page=1&keywords=ML2T_005/. A full list of MLS data can be found at http://disc.sci.gsfc.nasa.gov/Aura/dataholdings/. The MOHp lidar data can be freely downloaded from the NDACC data base (https://www-air.larc.nasa.gov/missions/ndacc/data.html).

6 Author statement

TT and HV carried out and evaluated the UFS lidar measurements. MB, CS and SW are responsible for the GRIPS observations, WS for the lidar measurements at MOHp. GN preselected and provided the MLS data. All authors contributed to preparing this manuscript.

7 Competing interests

The authors declare that they have no conflict of interest.

598 **Acknowledgements**

599 The authors from IMK-IFU thank Hans Peter Schmid for his support. Lisa Klanner (until 2015) and Matthias
600 Perfahl strongly contributed to the technical development of the system that recently has included remote
601 control. We are indepted to the considerable assistance of the UFS staff. The lidar development was funded by
602 the Bavarian Staatsministerium für Umwelt und Verbraucherschutz (BayStMUV). The GRIPS observations at
603 UFS have also been supported by BayStMUV in projects including GUDRUN, grant no. 71b-U8729-2003/125-
604 13; GRIPS3 Back-Up, 2009/40051; BHEA, TLK01U-49580; LUDWIG, TUS01UFS-67093; VoCaS,
605 TKP01KPB-70581; and AlpEn-DAC, TUS01UFS-72184). Gerald Nedoluha was supported by the NASA Earth
606 Sciences Division Upper Atmosphere Research Program and by the Office of Naval Research.
607

608 The service charges for this open access publication have been covered by a Research Centre of the Helmholtz
609 Association.

610 **References**

611 Alpers, M., Eixmann, R., Fricke-Begemann, C., Gerding, M., and Höffner, J.: Temperature lidar measurements
612 from 1 to 105 km altitude using resonance, Rayleigh, and Rotational Raman Scattering. Atmos. Chem. Phys.,
613 4,793–800, 2004.

614 Arnold, K. S., and She, C. Y.: Metal fluorescence lidar (light detection and ranging) and the middle atmosphere,
615 Contemp. Phys., 44, 35 – 49, 2003.

616 Arshinov, Y. F., Bobrovnikov, S. M., Zuev, V. E., and Mitev, V. M.: Atmospheric temperature measurements
617 using a pure rotational Raman lidar, Appl. Optics, 22, 2984–2990, 1983.

618 Baker, D. J. and Stair, A. T.: Rocket measurements of the altitude distributions of the hydroxyl airglow, Physica
619 Scripta, 37, 611–622, https://doi.org/10.1088/0031-8949/37/4/021, 1988.

620 Behrendt, A.: Temperature Measurements with Lidar, pp. 273-305 in: Lidar – Range-Resolved Optical Remote
621 Sensing of the Atmosphere, Claus Weitkamp, Ed., Springer Science and Business Media (New York, U.S.A.),
622 ISBN 0-387-40075-3, 2005.

623 Beig, G., Keckhut, P., Lowe, R. P., Roble, R. G., Mlynczak, M. G., Scheer, J., Fomichev, V. I., Offermann, D.,
624 French, W. J. R., Shepherd, M. G., Semenov, A. I., Remsberg, E. E., She, C. Y., Lübken, F. J., Bremer, J.,
625 Clemesha, B. R., Stegman, J., Sigernes, F., and Fadnavis, S.: Review of mesospheric temperature trends, Rev.
626 Geophys., 41, RG1015, https://doi.org/10.1029/2002RG000121, 2003.

627 Bittner, M., Offermann, D., and Graef, H. H.: Mesopause temperature variability above a midlatitude station in
628 Europe, J. Geophys. Res., 105, 2045-2058, 2000.

629 M. Bittner, M., Offermann, D., Graef, H.-H., Donner, M., and Hamilton, K.: An 18-year time series of OH
630 rotational temperatures and middle atmosphere decadal variations, J. Atmos. Solar-Terr. Phys., 64, 1147–1166,
631 2002.

632 Blamont, J. E., Chanin, M. L., and Mégie, G.: Vertical distribution and temperature profile of night time sodium
633 layer obtained by laser backscatter, Ann. Geophys., 26, 833-838, 1972.

634 Bowman, M. R., Gibson, A. J., and Sandford, M. C. W.: Atmospheric Sodium measured by a Tuned Laser
635 Radar, Nature, 221, 456-457, 1969.

636 Brinksma, E. J., Meijer, Y. J., McDermid, I. S., Cageao, R. P., Bergwerf, J. B., Swart, D. P. J., Ubachs, W.,
637 Matthews, W. A., Hogervorst, W., and Hovenier, J. W.: First lidar observations of mesospheric hydroxyl,
638 Geophys. Res. Lett., 25, 51-54, 1998; erratum: Geophys Res. Lett., 25, 521, 1998.

639 Bristow, M. P., Bundy, D. H., and Wright, A. G.: Signal linearity, gain stability, and gating in photomultipliers:
640 application to differential absorption lidars, Appl. Opt., 34, 4437-4452, 1996.

641 Carnuth, W., Kempfer, U., and Trickl, T.: Highlights of the tropospheric lidar studies at IFU within the TOR
642 project, Tellus B, 54, 163-185, 2002.

643 Chen, H., White, M. A., Krueger, D. A., and She, C. Y.: Daytime mesopause temperature measurements with a
644 sodium-vapor dispersive Faraday filter in a lidar receiver, Opt. Lett., 21, 1093-1095, 1996.

645 Chu, X., Gardner, C. S., and Papen, G.: Lidar Observations of Polar Mesospheric Clouds at South Pole: Diurnal
646 Variations, Geophys. Res. Lett., 28, 1937-1940, 2001.

647 Cooper, M.: Validation of SABER Temperature Measurements Using Ground-based Instruments, IGARSS
648 2004. 2004 IEEE International Geoscience and Remote Sensing Symposium, IEEE Xplore,
649 https://doi.org/10.1109/IGARSS.2004.1370033, 2004.

650 Curtis, R. D., Houghton, J. T., Peskett, G. D., and Rodgers, C. D.: The pressure modulator radiometer for
651 Nimbus F, Proc. R. Soc. London, A 337, 135-150, 1974.

652 Dawkins, E. C. M., Feofilov, A., Rezac, L., Kutepov, A. A., Janches, D., Höffner, J., Chu, X., Lu, X., Mlynczak,
653 M. G., and Russell, J. III: Validation of SABER v2.0 operational temperature data with ground-based lidars in
654 the mesosphere-lower thermosphere region (75−105 km). J. Geophys. Res., 123, 9916–9934, 2018.

655 Englert, C. R., Stevens, M. H., Siskind, D.- E., Harlander, J. M., and Roesler, F. L.: Spatial Heterodyne Imager
656 for Mesospheric Radicals on STPSat 1, J. Geophys. Res., 115, D20306, doi:10.1029/2010JD014398, 20 pp.,
657 2010.

658 Esplin, R., Mlynczak, M. G., Russell, J., Gordley, L., and The SABER Team: Sounding of the Atmosphere using
659 Broadband Emission Radiometry (SABER): Instrument and Science Measurement Description, Earth and Space
660 Science, 10, e2023EA002999, 32 pp., 2023.

661 Fishbein, E. F., Cofield, R. E., Froidevaud, L., Jarnot, R. F., Lungu, I. T., Read, W. G., Shippony, Z., Waters, J.
662 W., McDermid, I. S., McGee, T. J., Singh, U., Gross, M., Hauchecorne, A., Keckhut, P., Gelman, M. E., and
663 Nagatani, R. M.: Validation of UARS Microwave Limb Sounder temperature and pressure measurements, J.
664 Geophys. Res., 101, 9983-10016, 1996; the paper includes 353-nm measurements of the Table Mountain Facility
665 (McDermid et al., 1990).

666 Fricke, K. H., and von Zahn, U.: Mesopause temperatures derived from probing the hyperfine structure of the D_2
667 resonance line of sodium by lidar, J. Atmos. Terr. Phys., 47, 499-512, 1985.

668 Gerding, M., Höffner, J., Kopp, M., Eixmann, R., and Lübken, F.-J.: Mesospheric temperature and aerosol
669 soundings during day and night: spectra land spatial filtering techniques. in: 25th International Laser Radar
670 Conference, St. Petersburg, Russia, 2010, pp. 67–70, 2010.

671   Giehl, H., and Trickl, T.: Testing the IFU High-Spectral-Resolution Lidar at the 2009 Leipzig Field Campaign,
672   pp. 920-923 in: Proceedings of the 25th International Laser Radar Conference, St.-Petersburg (Russia), July 5 to
673   9, 2010, G. Matvienko, A. Zemlyanov, Eds., V. E. Zuev Institute of Optics (Tomsk, Russia), 2010.

674   Gille, S. T., Hauchecorne, A., and Chanin, M.-L.: Semidiurnal and diurnal tidal effects in the middle atmosphere
675   as seen by Rayleigh lidar, J. Geophys. Res., 96, 7579-7587, 1991.

676   Granier, C., Jegou, J. P., and Mégie, G.: Iron Atoms and Metallic Species in the Earth´s upper Atmosphere,
677   Geophys. Res. Lett., 16, 243-246, 1989.

678   Hannawald, P., Schmidt, C., Sedlak, R., Wüst, S., and Bittner, M.: Seasonal and intra-diurnal variability of
679   small-scale gravity waves in OH airglow at two Alpine stations, Atmos. Meas. Tech., 12, 457–469, 2019

680   Hauchecorne, A., and Chanin, M.-L.: Density and Temperature Profiles Obtained by Lidar between 33 and 70
681   km, Geophys. Res. Lett., 7, 565-568, 1980.

682   Hauchecorne, A., Chanin, M.-L., and Keckhut, P.: Climatology and Trends of the Middle Atmospheric
683   Temperature (33–87 km) as Seen by Rayleigh Lidar over the South of France, J. Geophys. Res., 96, 15297-
684   15309, 1991.

685   Höffner, J., and Lautenbach, J.: Daylight measurements of mesopause temperature and vertical wind with the
686   mobile scanning iron lidar, Opt. Lett. 34, 1351-1353 (2009)

687   Höveler, K.: Entwicklung eines Nahbereichsempfängers zur Messung von Wasserdampf- und Temperaturpro-
688   filen für das Hochleistungs-Raman-Lidar am Schneefernerhaus, Masterarbeit, Karlsruher Institut für
689   Technologie, Fakultät für Physik, 138 pp., 2015 (in German).

690   Iarlori, M., Madonna, F., Rizi, V., Trickl, T., and Amodeo, A.: Effective resolution concepts for lidar
691   observations, Atmos. Meas. Tech., 8, 5157–5176, https://doi.org/10.5194/amt-8-5157-2015, 2015.

692   Jäger, H. and Deshler, T.: Lidar backscatter to extinction, mass and area conversions for stratospheric aerosols
693   based on midlatitude, Geophys. Res. Lett., 29, 1929, 2002.

694   Jäger, H. and Deshler, T.: Correction to "Lidar backscatter to extinction, mass and area conversions for
695   stratospheric aerosols based on midlatitude balloonborne size distribution measurements", Geophys. Res. Lett.,
696   30, 1382, 2003.

697   Keckhut, P.: Middle atmospheric temperature measurements with lidar, J. Physique, 121, 239–248, 2004.

698   Khanna, J., Bandoro, J., Sica, R. J., and McElroy, C. T.: New technique for retrieval of atmospheric temperature
699   profiles from Rayleigh-scatter lidar measurements using nonlinear inversion, Appl. Opt., 51, 7945-7852, 2012.

700   Kim, Y.-J., Eckermann, S. D., and Chun, H.-Y.: An overview of the past, present and future of gravity wave
701   drag parametrization for numerical climate and weather prediction models. Atmosphere-Ocean, 41, 65-98, 2003.

702   Klanner, L.: Entwicklung eines Hochleistungs-Raman-Lidars für die Messung von Wasserdampf- und
703   Temperaturprofilen in der Atmosphäre, Technische Universität München, Fakultät Wissenschaftszentrum
704   Weihenstephan, Dissertation, 186 pp., 2022 (in German).

705   Klanner, L., Höveler, K., Khordakova, D., Perfahl, M., Rolf, C., Trickl, T., and Vogelmann, H.: A powerful lidar
706   system capable of 1 h measurements of water vapour in the troposphere and the lower stratosphere as well as the
707   temperature in the upper stratosphere and mesosphere, Atmos. Meas. Tech., 14, 531-555, 2021.

708   Klett, J. D.: Stable analytical inversion solution for processing lidar returns, Appl. Opt., 20, 211-220, 1981.

709 Klett, J. D.: Lidar inversion with variable backscatter/extinction ratios, Appl. Opt., 24, 1638-1643, 1985.

710 Kopp, M., Gerding, M., Höffner, J., and Lübken, F.-J.: Tidal signatures in temperatures derived from daylight
711 lidar soundings above Kühlungsborn (54°N, 12°E), J. Atmos. Sol.-Terr. Phys., 127, 37–50, 2015.

712 Kreipl, S.: Messung des Aerosoltransports am Alpennordrand mittels Laserradar (Lidar), Dissertation, Friedrich-
713 Alexander-Universität Erlangen-Nürnberg (Germany), 195 pp., 2006 (in German); the relevant figure can be
714 found at http://www.trickl.de/PMT.PDF.

715 Leblanc, T., McDermid, I. S., Keckhut, P., Hauchecorne, A., She, C. Y., and Krueger, D. A.: Temperature
716 climatology of the middle atmosphere from long-term lidar measurements at middle and low latitudes, J.
717 Geophys. Res., 103, 17191-17204, 1998

718 Leblanc, T., Sica, R. J., van Gijsel, J. A. E., Godin-Beekmann, S., Haefele, A., Trickl, T., Payen, G., and
719 Gabarrot, F.: Proposed standardized definitions for vertical resolution and uncertainty in the NDACC lidar ozone
720 and temperature algorithms – Part 1: Vertical resolution, Atmos. Meas. Tech., 9, 4029–4049,
721 https://doi.org/10.5194/amt-9-4029-2016, 2016.6.

722 Liu, G. and Shepherd, G. G.: An empirical model for the altitude of the OH nightglow emission, Geophys. Res.
723 Lett., 33, L09805, https://doi.org/10.1029/2005gl025297, 2006.

724 Li, A., Roth, C. Z., Bourassa, A. E., Degenstein, D. A., Pérot, K., Christensen, O. M., and Murtagh, D. P.: The
725 OH (3-1) nightglow volume emission rate retrieved from OSIRIS measurements: 2001 to 2015. Earth Syst. Sci.
726 Data, 13(11), 5115-5126, https://doi.org/10.5194/essd-13-5115-2021, 2021.

727 Lopez-Moreno, J. J., Rodrigo, R., Moreno, F., Lopez-Puetas, M., and Molina, A.: Altitude distribution of
728 vibrationally excited states of atmospheric hydroxyl at levels v = 2 to v = 7, Planet. and Space Sci., 35(8), 1029-
729 1038, https://doi.org/10.1016/0032-0633(87)90007-9, 1987.

730 McDermid, I. S., Godin, S. M., and Walsh, T. D.: Lidar measurements of stratospheric ozone and
731 intercomparisons and validation, Appl. Opt., 29, 4914-4923, 1990.

732 Medvedev, A. S., and Yiğit, E.: Gravity waves in planetary atmospheres: Their effects and parameterization in
733 global circulation models. Atmosphere, 10, 531, 2019.

734 Medvedewa, I. V., Semenov, A. I., Perminov, V. I., Beletsky, A. B., and Tartarnikov, A. V.: Comparison of
735 Ground-based OH Temperature Data Measured at Irkutsk (52°N, 103°E) and Zvenigorod (56°N, 37°E) Stations
736 with Aura MLS v3.3, 62, pp. 340-349, DOI: 10.2478/s11600-013-0161-x, 2014.

737 Mégie, G., Bos, F., Blamont, J. E., and Chanin, M. L.: Simultaneous Nighttime Measurements of Sodium and
738 Potassium, Planet. Space Sci., 26, 27-35, 1978.

739 Mertens, C. J., Russell, J. M. III, Mlynczak, M. G., She, C,-Y., Schmidlin, F. J., Richard A. Goldberg, R. A.,
740 López-Puertas, M., Wintersteiner, P. P., Picard, R. H., Winick, J. R., and Xu, X.: Kinetic temperature and carbon
741 dioxide from broadband infrared limb emission measurements taken from the TIMED/SABER instrument, Adv.
742 Space Res., 43, 15–27, 2009.

743 Mulligan, F., Horgan, D., Galligan, J., and Griffin, E.: Mesopause temperatures and integrated band brightnesses
744 calculated from airglow OH emissions recorded at Maynooth (53.2° N, 6.4° W) during 1993, J. Atmos. Terr.
745 Phys., 57, 1623–1637, 1995.

746 Mohr, P. J., Newell, D. B., and Taylor, B. N.: CODATA recommended values of the fundamental physical
747 constants: 2014, Rev. Modern Phys., 88, 035009, 73 pp., 2016.

748 Nedoluha, G. E. , Gomez, R. M., Boyd, I. , Neal, H., Allen, D. R., and Lambert, A.: The Spread of the Hunga
749 Tonga H_2O Plume in the Middle Atmosphere Over the First Two Years Since Eruption, J. Geophys. Res., 129,
750 e2024JD040907. https://doi.org/10. 1029/2024JD0409, 11 pp., 2024.

751 Nedoluha, G. E. , Gomez, R. M., Boyd, I. , Neal, H., Allen, D. R., Parrish, A., Connor, B.- J., and Siskind, D. E.:
752 Measurements of Stratospheric ClO From Mauna Kea: 1992–2023, J. Geophys. Res., 130, e2024JD041848.
753 https://doi.org/10.1029/2024JD041848, 13 pp., 2025.

754 Noll, S., Kimeswenger, S., Proxauf, B., Unterguggenberger, S., Kausch, W., and Jones, A. M.: 15 years of
755 VLT/UVES OH intensities and temperatures in comparison with TIMED/SABER data, J. Atmos. Sol.-Terr.
756 Phys., 163, 54–69, 2017.

757 Noll, S., Winkler, H., Goussev, O., and Proxauf, B.: OH level populations and accuracies of Einstein-A
758 coefficients from hundreds of measured lines, Atmos. Chem. Phys., 20, 5269–5292, 2020.

759 Noll, S., Schmidt, C., Kausch, W., Bittner, M., and Kimeswenger, S.: Climatologies of various OH lines from
760 about 90,000 X-shooter spectra, J. Geophys. Res., 128, https://doi.org/10.1029/2022JD038275, 2023.

761 Ott, H.: Single atom detection in ultracold quantum gases: a review of current progress, Rep. Prog. Phys., 79,
762 054401, 2016.

763 Papen, G. C., Pfenninger, W. M., and Simonich, D. M.: Sensitivity analysis of Na narrowband wind-temperature
764 lidar systems, Appl. Opt., 34, 480-498, 1995.

765 Piironen, P., and Eloranta, E. W.: Demonstration of a high-spectral-resolution lidar based on an iodine
766 absorption filter, Opt. Lett., 19, 234-236, 1994.

767 Reisin, E. R., Scheer, J., Dyrland, M. E., Sigernes, F., Deehr, C. S., Schmidt, C., Höppner, K., Bittner, M.,
768 Ammosov, P. P., Gavrilyeva, G. A., Stegman, J., Perminov, V. I., Semenov, A. I., Knieling, P., Koppmann, R.,
769 Shiokawa, K., Lowe, R. P., López-González, M. J., Rodríguez, E., Zhao, Y., Taylor, M. J., Buriti, R. A., Espy, P.
770 J., French, W. J. R., Eichmann, K.-U., Burrows, J. P., and von Savigny, C.: Traveling planetary wave activity
771 from mesopause region airglow temperatures determined by the Network for the Detection of Mesospheric
772 Change (NDMC), J. Atmos. Sol.-Terr. Phys., 119, 71–82, 2014.

773 Russell, J. M. III, Mlynczak, M. G., Gordley, L. L., Tansock, J., and Esplin, R.: An overview of the SABER
774 experiment and preliminary calibration results, Proc. SPIE, 3756, 277-288, 1999.

775 Scheer, J., Reisin, E. R., Espy, J. P., Bittner, M., Graef, H. H., Offermann, D., Ammoso, P. P., and Ignatyev, V.
776 M.: Large-scale structures in hydroxyl rotational temperatures during DYANA, J. Atmos. Terr. Phys., 56, 1701-
777 1715, 1994.

778 Schmidt, C., Höppner, K., and Bittner, M.: A ground-based spectrometer equipped with an InGaAs array for
779 routine observations of OH (3-1) rotational temperatures in the mesopause region, J. Atmos. Sol.-Terr. Phys.,
780 102, 125–139 2013.

781 Schmidt, C., Dunker, T., Lichtenstern, S., Scheer, J., Wüst, S., Hoppe, U.-P., and Bittner M.: Derivation of
782 vertical wavelengths of gravity waves in the MLT-region from multispectral airglow observations, J. Atmos.
783 Sol.-Terr. Phys., 173, 119-127, https://doi.org/10.1016/j.jastp.2018.03.002, 2018.

784 Schmidt, C., Küchelbacher, L., Wüst, S., and Bittner, M.: OH airglow observations with two identical
785 spectrometers: benefits of increased data homogeneity in the identification of variations induced by the 11-year

solar cycle, the QBO, and other factors. Atmos. Meas. Tech. 16, 4331-4356, https://doi.org/10.5194/amt-16-4331-2023, 2023.

Schoeberl, M. R., Douglass, A. R., Hilsenrath, E., Bhartia, P. K., Beer, R., Waters, J. W., Gunson, M. R., Froidevaux, L., Gille, J. C., Barnett, J. J., Levelt, P. F., and DeCola, P.: Overview of the EOS Aura mission, IEEE Trans. Geosci. Remote Sens., 44, 1066–1074, 2006.

Schwartz, M. L., Lambert, A., Manney, G. L;, Read, W. G., Livesey, N. E., J., Froidevaux, L., Ao, C. O., Bernath, P. F., Boone, C. D., Cofield, R. E., Daffer, W. H., Drouin, B. J., Fetzer, E. J., Fuller, R. A., Jarnot, R. F., Jiang, J. H., Jiang, Y. B., Knosp, B. W., Krüger, K., Li, J.-L. F., Mlynczak, M. G., Pawson, S., Russell, J. M. III, Santee, M. L., Snyder, W. V., Stek, P. C., Thurstans, R. P., Tompkins, A. M., Wagner, P. A., Walker, K. A., Waters, J. W., and Wu, D. L.: Validation of the Aura Microwave Limb Sounder temperature and geopotential height measurements, J. Geophys. Res., 113, D15S11, doi: 10.1029/2007JD008783, 23 pp., 2008.

Serikov, I., and Bobrinikov, S.: Atmospheric temperature profiling with pure rotational Raman lidars, pp. 149-216, Series: Optoelectronic Materials and Devices, Vol. 7, Recent Advances in Atmospheric Lidars, L. Fiorani, and V. Mitev, Eds., National Institute of Research and Development for Optoelectronics (Bucharest, Romania), ISBN 978-973-88109-6-9, 2009.

She, C. Y., and Lowe, R.P.: Seasonal temperature variations in the mesopause region at mid-latitudes: Comparison of lidar and hydroxyl rotational temperatures using WINDII/UARS OH height profiles, J. Atmos. Solar-Terr. Phys., 60, 1573–1583, 1998.

She, C. V., Lativi, H., Yu, Y. R., Alvarez II, R. J., Bills, R. E., and Gardner, C. S.: Two-frequency Lidar Technique for Mesospheric Na Temperature Measurements, Geophys. Res. Lett., 17, 929-932, 1990.

Shibata, T., Kobuchi, M., and Maeda, M.: Measurements of density and temperature profiles in the middle atmosphere with a XeF lidar, Appl. Optics, 25, 685–688, 1986.

Sica, R. J., Measurements of the Effects of Gravity Waves in the Middle Atmosphere Using Parametric Models of Density Fluctuations. Part II: Energy Dissipation and Eddy Diffusion, J. Atmos. Sci., 56, 1330-1343, 1999.

Sica, R. J., Sargoytchev, S., Argall, P. S., Borra, E. F., Girard, L., Sparrow, C. T., and Flatt, S.: Lidar measurements taken with a large-aperture liquid mirror. 1. Rayleigh-scatter system, Appl. Opt., 34, 6925-6936, 1995.

Sivjee, G. G.: Airglow Hydroxyl Emissions, Planet. Space Sci., 40, 235–242, 1992.

Steinbrecht, W ., Velazco, V. A., Dirksen, R., Doppler, L., Oelsner, P., Van Malderen, R., De Backer, H., Maillard Barras, E., Stübi, R., Godin-Beekmann, S., and Hauchecorne, A.: Ground-Based Monitoring of Stratospheric Ozone and Temperature Over Germany Since the 1960s, Earth Space Sci., 12, e2024EA003821, 24 pp., https://doi.org/10.1029/2024, 2025.

Takahashi, H., Clemesha, B. R., Simonich, D. M., Melo, S. M. L., Teixeira, N. R., Eras, A., Stegman, J., Witt, G.: Rocket measurements of the equatorial airglow: MULTIPHOT 92 database, J. Atmos. Terr. Phys., 58, 1943–1961, 1996.

Trickl, T.: Upgraded 1.56-μm lidar at IMK-IFU with 0.28 J/pulse, Appl. Opt., 49, 3732-3740, 2010.

Trickl, T., Giehl, H., Jäger, H., and Vogelmann, H.: 35 years of stratospheric aerosol measurements at Garmisch-Partenkirchen: from Fuego to Eyjafjallajökull, and beyond, Atmos. Chem. Phys., 13, 5205-5225, 2013.

824 Trickl, T., Vogelmann, H., Giehl, H., Scheel, H. E., Sprenger, M., and Stohl, A.: How stratospheric are deep
825 stratospheric intrusions? Atmos. Chem. Phys., 14, 9941-9961, 2014.

826 Trickl, T., Vogelmann, H., Flentje, H., and Ries, L.: Stratospheric ozone in boreal fire plumes – the 2013 smoke
827 season over Central Europe, Atmos. Chem. Phys., 15, 9631-9649, 2015.

828 Trickl, T., Vogelmann, H., Fix, A., Schäfler, A., Wirth, M., Calpini, B., Levrat, G., Romanens, G., Apituley, A.,
829 Wilson, K. M., Begbie, R., Reichardt, J., Vömel, H. and Sprenger, M.: How stratospheric are deep stratospheric
830 intrusions into the troposphere? LUAMI 2008, Atmos. Chem. Phys, 16, 8791-8815, 2016.

831 Trickl, T., Neidl, F., Giehl, H., Perfahl, M., and Vogelmann, H.: Three decades of tropospheric ozone lidar
832 development at Garmisch-Partenkirchen, Atmos. Meas. Tech., 13, 6357-6390, 2020.

833 Trickl, T., Adelwart, M., Khordakova, D., Ries, L., Rolf, C., Steinbrecht, W., and Vogelmann, H.: Local
834 comparisons of tropospheric ozone: Vertical sounding at two neighbouring stations in Southern Bavaria, Atmos.
835 Meas. Tech. 16, 5145–5165. 2023.

836 Trickl, T., Vogelmann, H., Fromm, M. F., Jäger, H., Perfahl, M., and Steinbrecht, W.: Measurements report:
837 Violent biomass burning and volcanic eruptions: a new period of elevated stratospheric aerosol over Central
838 Europe (2017 to 2023) in a long series of observations, Atmos. Chem. Phys., 24, 1997-2021, 2024.

839 U.S. Standard Atmosphere: National Oceanic and Atmospheric Organization (NOAA), National Aeronautics and
840 Space Administration, United States Air Force, NOAA-S/T 76-1562, US Printing Office (Washington, D.C.),
841 227 pp., 1976.

842 VDI: guide line 4210 Remote Sensing, Atmospheric Measurements with LIDAR, Measuring gaseous air
843 pollution with the DAS LIDAR, Verein Deutscher Ingenieure, Düsseldorf, Germany, 47 pp., 1999.

844 Vogelmann, H. and Trickl, T.: Wide-Range Sounding of Free-Tropospheric Water Vapor with a Differential-
845 Absorption Lidar (DIAL) at a High-Altitude Station, Appl. Opt., 47, 2116-2132, 2008.

846 Vogelmann, H., Sussmann, R., Trickl, T., and Borsdorff, T.: Intercomparison of atmospheric water vapor
847 soundings from the differential absorption lidar (DIAL) and the solar FTIR system on Mt. Zugspitze, Atmos.
848 Meas. Tech., 4, 835-841, 2011.

849 Von Savigny, C., McDade, I. C., Eichmann, K.-U., and Burrows, J. P.: On the dependence of the OH* Meinel
850 emission altitude on vibrational level: SCIAMACHY observations and model simulations, Atmos. Chem. Phys.,
851 12, 8813–8828, 2012.

852 Von Savigny, C. and Lednyts'kyy, O.: On the relationship between atomic oxygen and vertical shifts between
853 OH Meinel bands originating from different vibrational levels, Geophys. Res. Lett. 40, 5821–5825.
854 https://doi.org/10.1002/2013GL058017, 2013.

855 Von Zahn, U., Fricke, K. H, Gerndt, R., and Blix, T.: Mesospheric temperatures and the OH layer height as
856 derived from ground-based lidar and OH* spectrometry, J. Atmos. Terr. Phys., 38, 49, 863–869, 1987.

857 Von Zahn, U., von Cossart, G., Fiedler, J., Fricke, K. H., Nelke, G., Baumgarten, G., Rees, D., Hauchecorne, A.,
858 and Adolfsen, K.: The ALOMAR Rayleigh/Mie/Raman lidar: objectives, configuration, and performance, Ann.
859 Geophysicae, 18, 815-833, 2000.

860 Waters, J. W., Froidevaux, L., Harwood, R. S., Jarnot, R. F., Pickett, H. M., Read, W. G., Siegel, P. H., Cofield,
861 R. E., Filipiak, M. J., Flower, D. A., Holden, J. R., Lau, G. K., Livesey, N. J., Manney, G. L., Pumphrey, H. C.,

Santee, M. L., Wu, D. L., Cuddy, D. T., Lay, R. R. Loo, M. S., Perun, V. S., Schwartz, M. J., Stek, P. C., Thurstans, R. P., Boyles, M. A., Chandra, K. M., Chavez, M. C., Chen, G.-S., Chudasama, B. V., Dodge, R., Fuller, R. A., Girard, M. A., Jiang, J. H., Jiang, Y. Knosp, B. W., LaBelle, R. C., Lam, J. C., Lee, K. A., Miller, D., Oswald, J. E., Patel, N. C., Pukala, D. M., Quintero, O., Scaff, D. M., Van Snyder, W. Tope, M. C., Wagner, P. A., and Walch M. J.: The Earth Observing System Microwave Limb Sounder (EOS MLS) on the Aura satellite, IEEE Trans. Geosci. Remote Sens., 44, 1075–1092, 2006.

Wandinger, U., Freudenthaler, V., Baars, H., Amodeo, A., Engelmann, R., Mattis, I., Groß, S., Pappalardo, G., Giunta, A., D'Amico, G., Chaikovsky, A., Ossipenko, F., Slesar, A., Nicolae, D., Belegante, L., Talianu, C., Serikov, I., Linné, H., Jansen, F., Apituley, A., Wilson, K., de Graaf, M., Trickl, T., Giehl, H., Adam, M., Comeron, A., Muñoz-Porcar, C., Rocadenbosch, F., Sicard, M., Tomás, S., Lange, D., Kumar, D., Pujadas, M., Molero, F., Fernandez, A. J., Alados Arboledas, L., Bravo-Aranda, J. A., Navas-Guzmán, F., Guerrero-Rascado, J, L., Granados-Munoz, M. J.. Preißler, J., Wagner, F., Gausa, M., Grigorov, I., Stoyanov, D., Iarlori, M., Rizi, V., Spinelli, N., Boselli, A., Wang, X., Lo Feudo, T., Perrone, M. R., De Tomasi, F., and Burlizzi, P.: EARLINET instrument intercomparison campaigns: Overview on strategy and results, Atmos. Meas. Tech., 9, 1001-1023, 2016.

Wing, R., Hauchecorne, A., Keckhut, P., Godin-Beekmann, S., Khaykin, S., McCullough, E. M., Mariscal, J.-F. and d'Almeida, E.: Lidar temperature series in the middle atmosphere as a reference data set – Part 1: Improved retrievals and a 20-year cross-validation of two co-located French lidars, Atmos. Meas. Tech., 11, 5531–5547, 2018a.

Wing, R., Hauchecorne, A., Keckhut, P., Godin-Beekmann, S., Khaykin, S., and McCullough, E. M.: Lidar temperature series in the middle atmosphere as a reference data set – Part 2: Assessment of temperature observations from MLS/Aura and SABER/TIMED satellites, Atmos. Meas. Tech., 11, 6703–6717, 2018b.

Wing, R., Godin-Beekmann, S., Steinbrecht, W., McGee, T. J., Sullivan, J. T., Khaykin, S., Sumnicht, G., and Twigg, L.: Evaluation of the new DWD ozone and temperature lidar during the Hohenpeißenberg Ozone Profiling Study (HOPS) and comparison of results with previous NDACC campaigns, Atmos. Meas. Tech., 14, 3773–3794, 2021

Wüst, S., Bittner, M., Yee, Y.-H., Mlynczak, M. G., and Russell, J. M. III: Variability of the Brunt–Väisälä frequency at the OH* layer height, Atmos. Meas. Tech., 10, 4895–4903, https://doi.org/10.5194/amt-10-4895-2017, 2017.

Wüst, S., Bittner, M., Yee, J.-H., Mlynczak, M. G., and Russell III, J. M.: Variability of the Brunt–Väisälä frequency at the OH∗-airglow layer height at low and midlatitudes, Atmos. Meas. Tech., 13, 6067–6093, https://doi.org/10.5194/amt-13-6067-2020, 2020.

Wüst, S., Bittner, M., Espy, P. J., French, P. J., and Mulligan, F.- J.: Hydroxyl airglow observations for investigating atmospheric dynamics: results and challenges, Atmos. Chem. Phys., 23, 1599-1618, https://doi.org/10.5194/acp-23-1599-2023, 2023.

Xu, J., She, C. Y., Yuan, W., Mertens, C., Mlynczak, M., and Russell, J.: Comparison between the temperature measurements by TIMED/SABER and lidar in the midlatitude, J. Geophys. Res., 111, A10S09, doi: 10.1029/2005JA011439, 11pp., 2006.

     Figures:

902

903
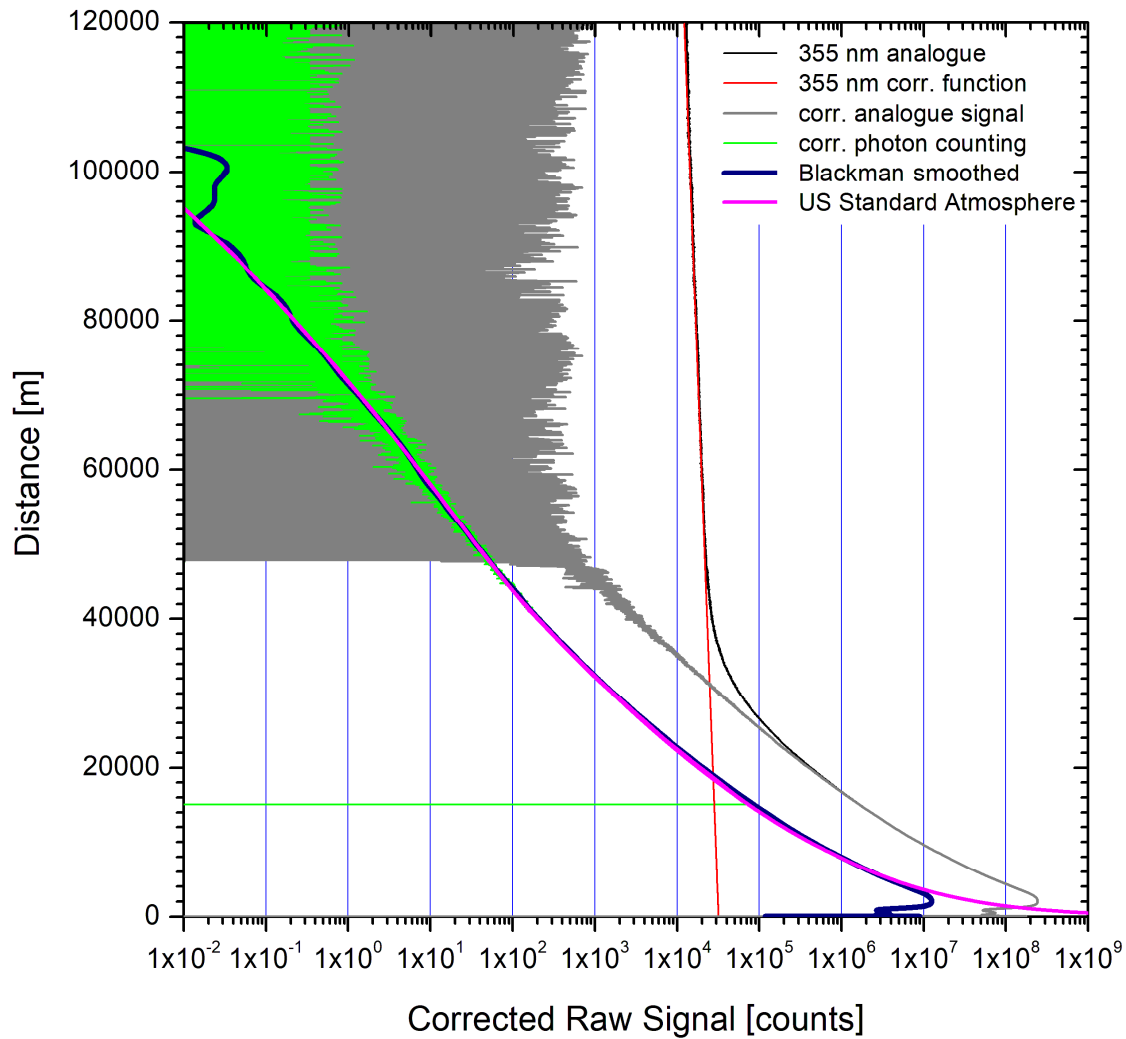
904   **Fig. 1.** 355-nm backscatter signals accumulated on 9 October 2021 between 23:05 and 24:01 CET (67171 laser
905   shots) with the transient digitizer (black; corrected: grey) and the photon-counting system (light green); the
906   photon-counting signal starts at 15 km due to a data-acquisition delay (see horizontal green line). Above 100 km
907   just occasionally a single photon was detected (see scale). The combined signal (after calibrating the analogue
908   signal to counts) from both recorders is smoothed with a Blackman-type numerical filter with a range
909   quadratically growing with altitude (blue; see text in Sect. 3.1). For comparison also a synthetic lidar signal
910   simulated with data from the U.S. Standard Atmosphere is shown.

911

912
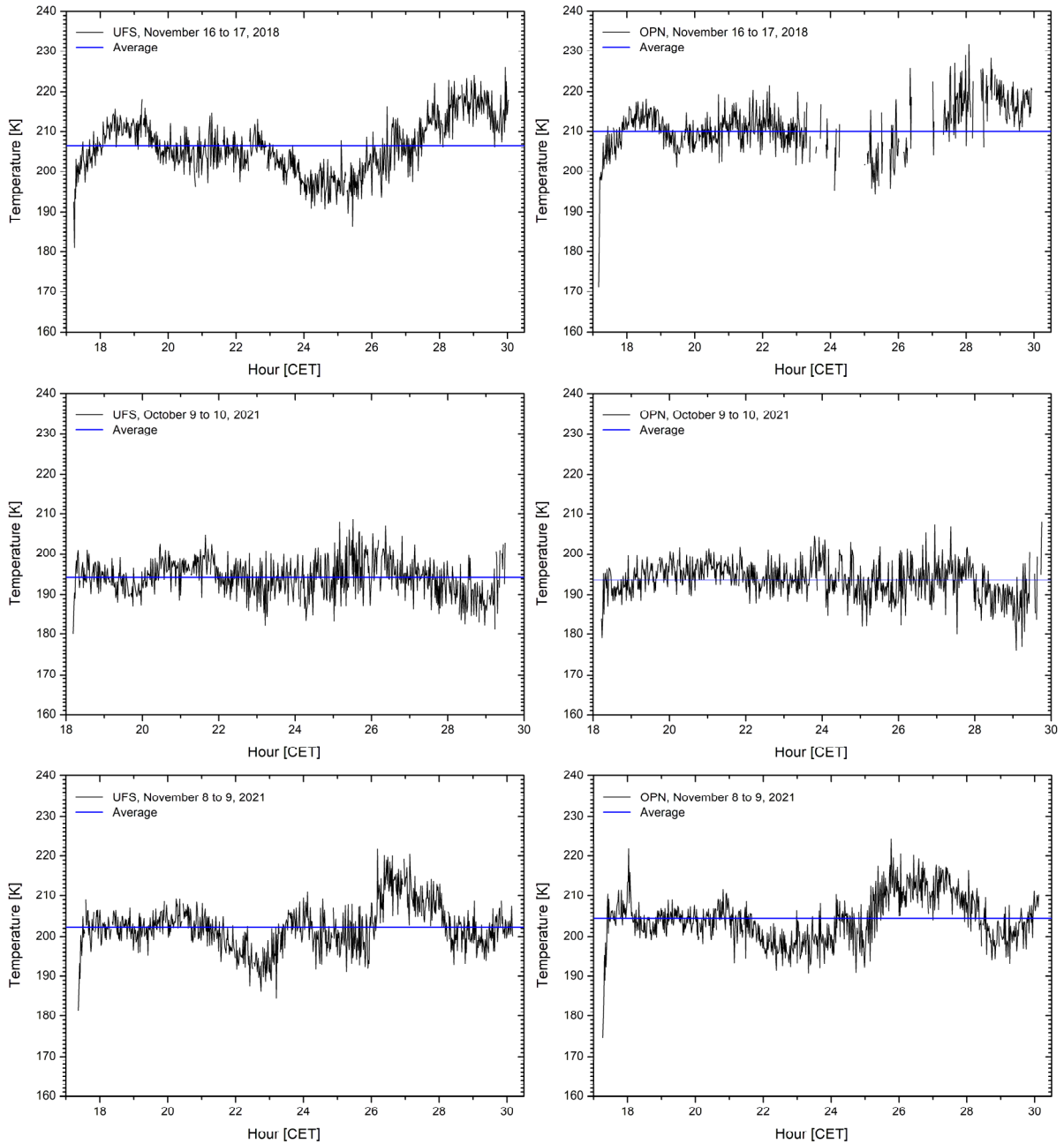
913 **Fig. 2.** Examples of GRIPS night-time temperature series at UFS (left column) and Oberpfaffenhofen (OPN,
914 right column) in November 2018, October 2021 and November 2021. There is relatively good agreement for the
915 first two measurements, but in the third case some differences are seen between the results of the two stations.
916 Gaps are due to cloud coverage. The uncertainties at the beginning and the end of a given night is high due to
917 additional daylight.
918
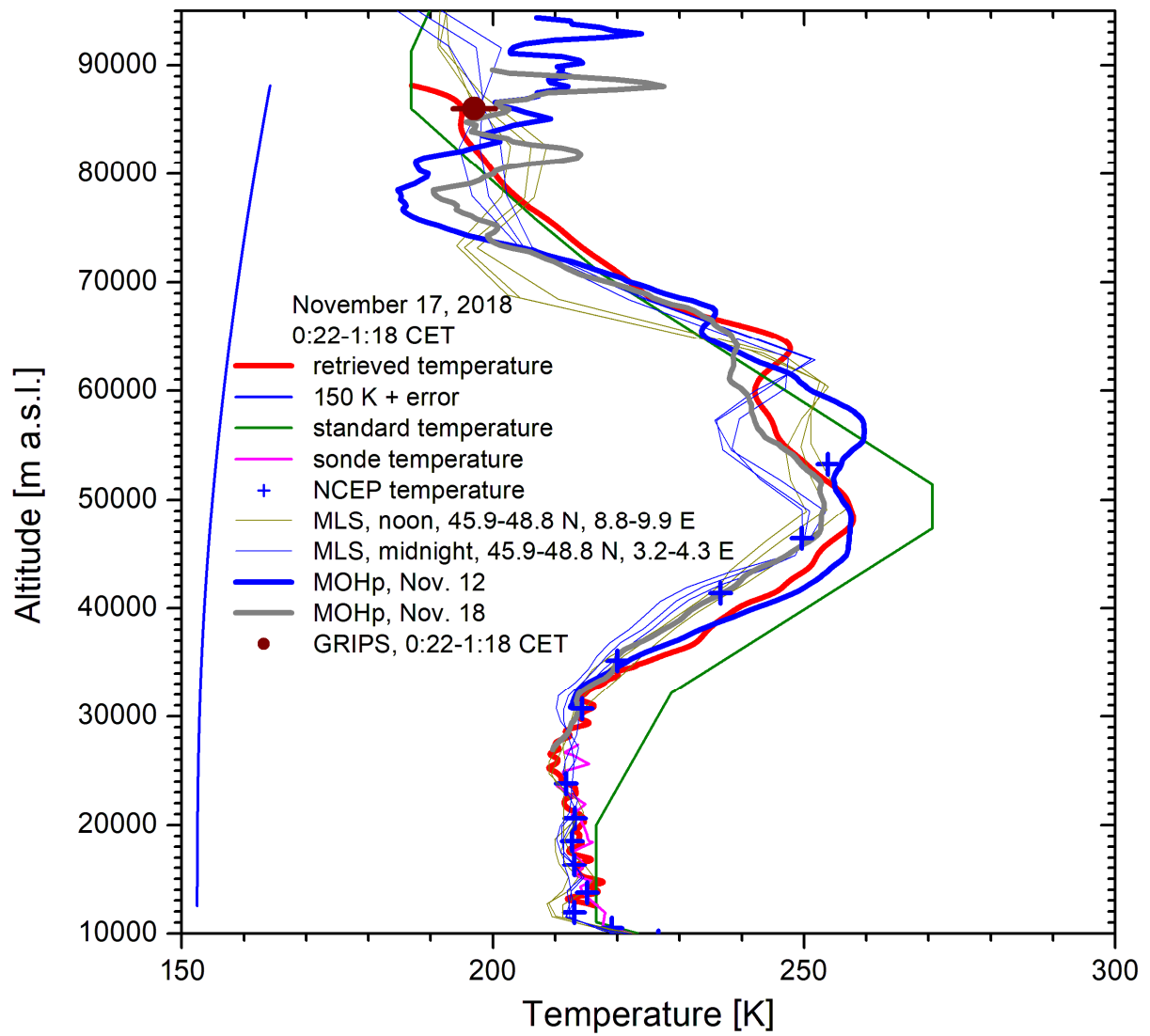
919
920 **Fig. 3.** Temperature measurements on 17 November 2018, compared with data and profiles from other sources

921 (see text).

922
923 **Please, print this figure larger than in single-column format to allow visualizing the details.**

924

925
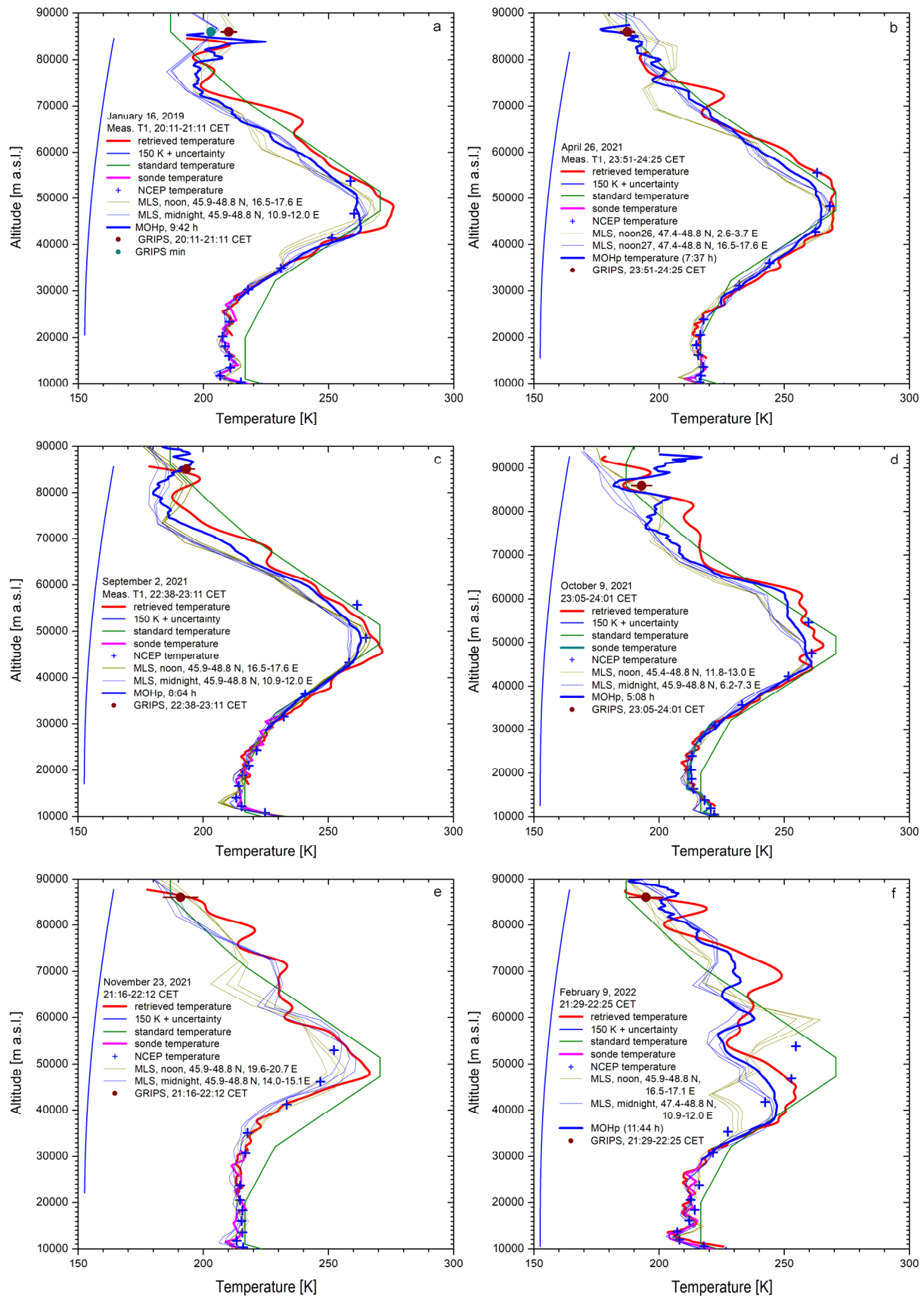
Fig. 4. Six examples of comparisons of temperature profiles from the UFS lidar with the results of other instruments (for details see legends and text). For a given day, we show both the "midnight" and the "noon" MLS profiles. In the case of Panel (b) the "midnight" MLS profiles are missing and those of the neighbouring two "noon" overpasses are displayed.

926
927
928
929
930
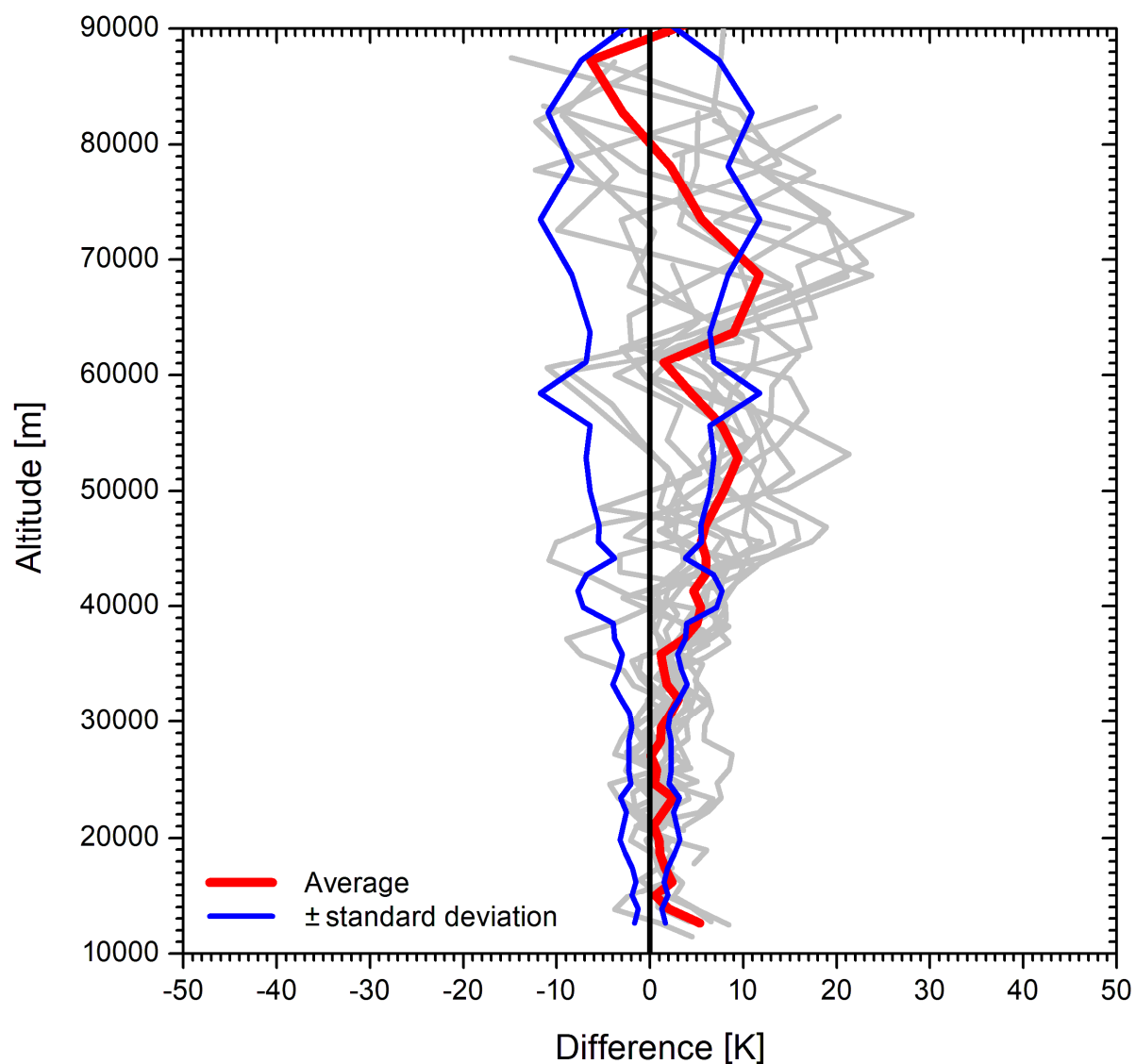
Fig. 5. Differences of the 14 temperature profiles of the UFS lidar and the corresponding measurements of MLS

for 47.35º N (grey lines) together with their averages (red line) and standard deviations (blue lines).

935
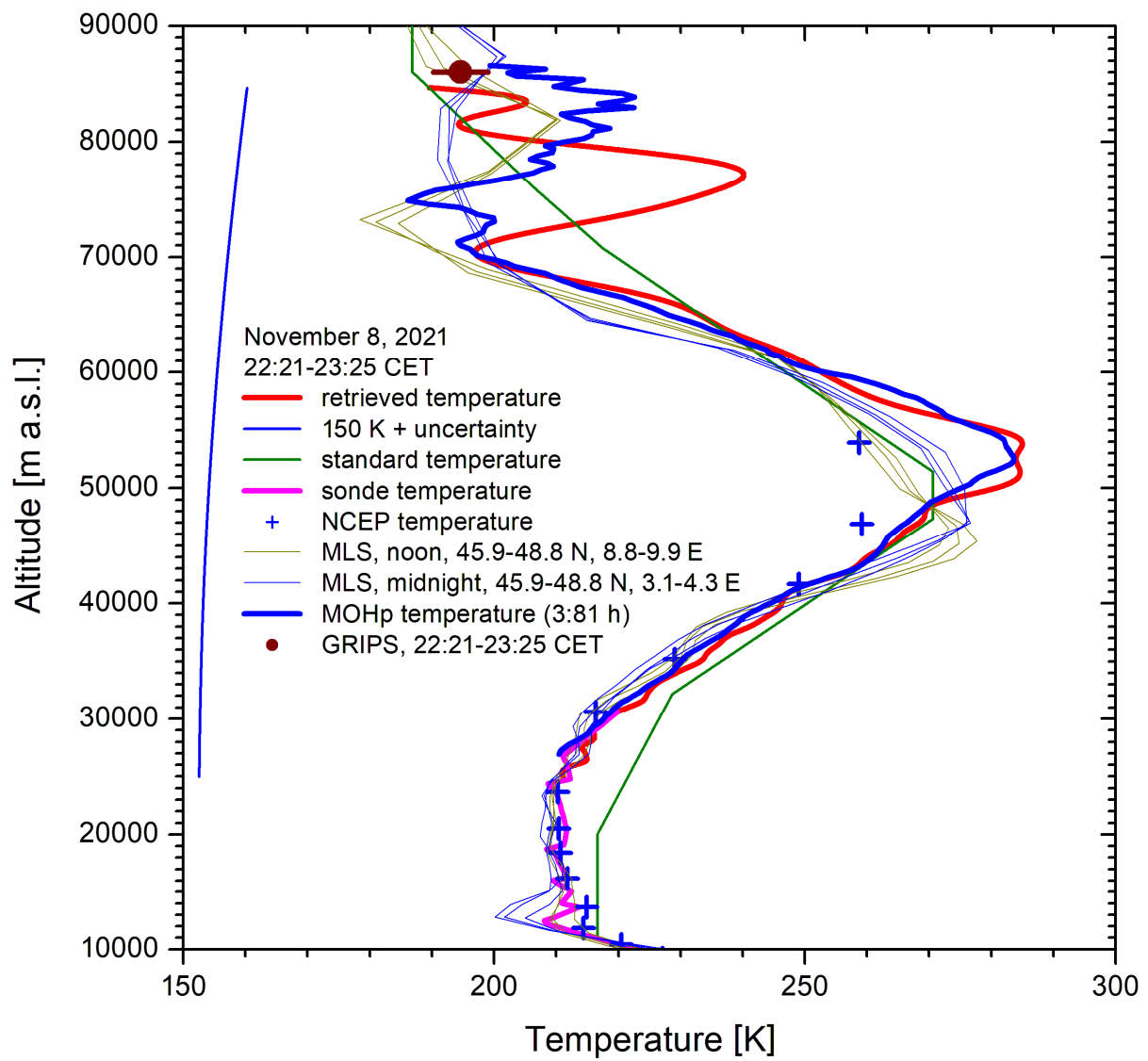
Fig. 6. Comparison of the temperature profile from the UFS lidar on 8 November 2021 with the results of other instruments; here, we observe an almost perfect agreement with the T profile from MOHp up to 70 km, that was taken during a rather short period between 22:30 CET and 1:49 CET, i.e., almost synchronously to the measurement at UFS.
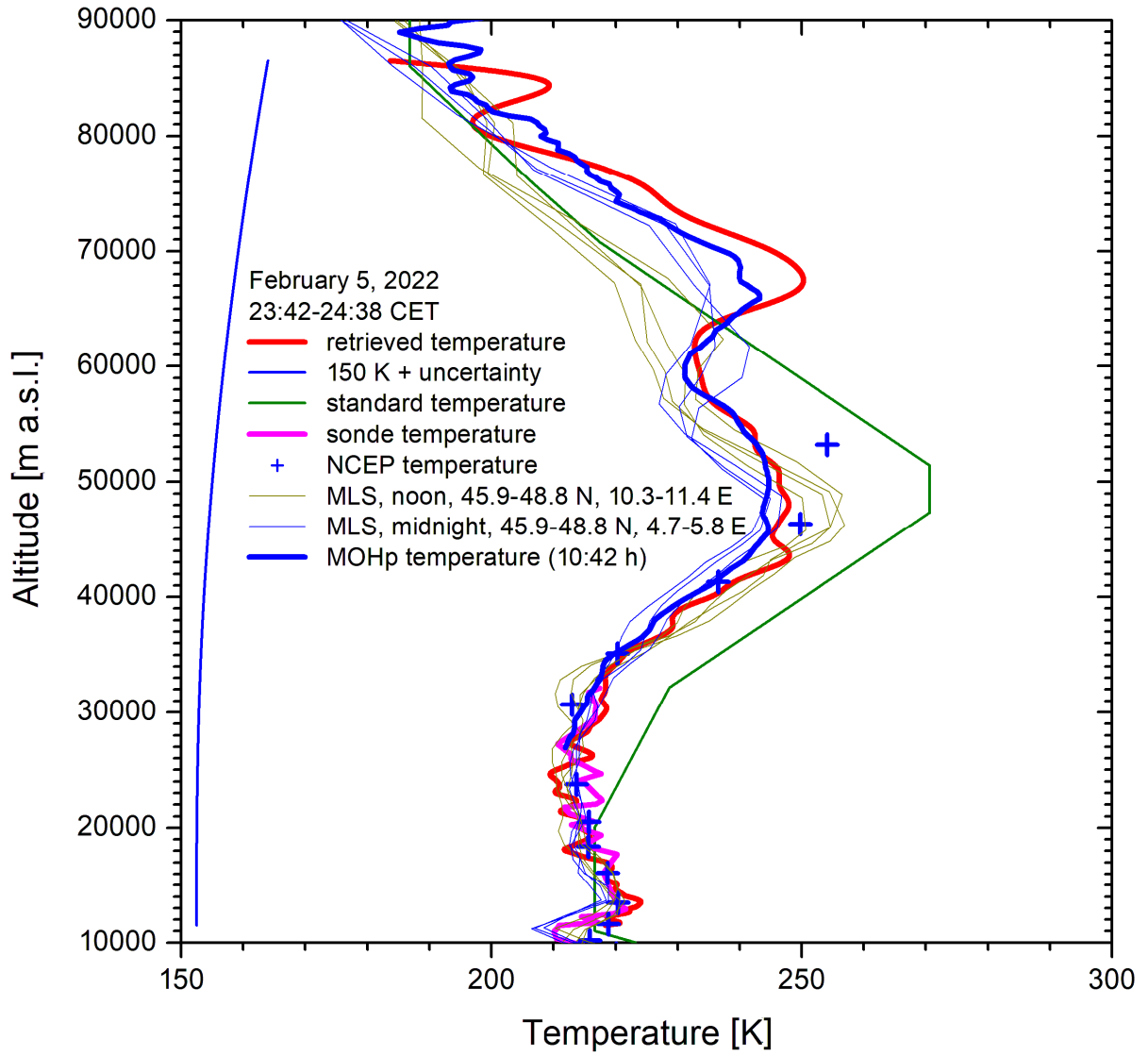
 Fig. 7. Comparison of the temperature profile from the UFS lidar on 5 February 2022 with the results of other

943 instruments; here, we observe an almost perfect agreement with the T profile from MOHp, showing rather good

944 agreement up to 65 km. No OH* measurements are available for that night. The reference temperature was

945 chosen to ensure an average temperature matching with MOHp above 77 km.

946
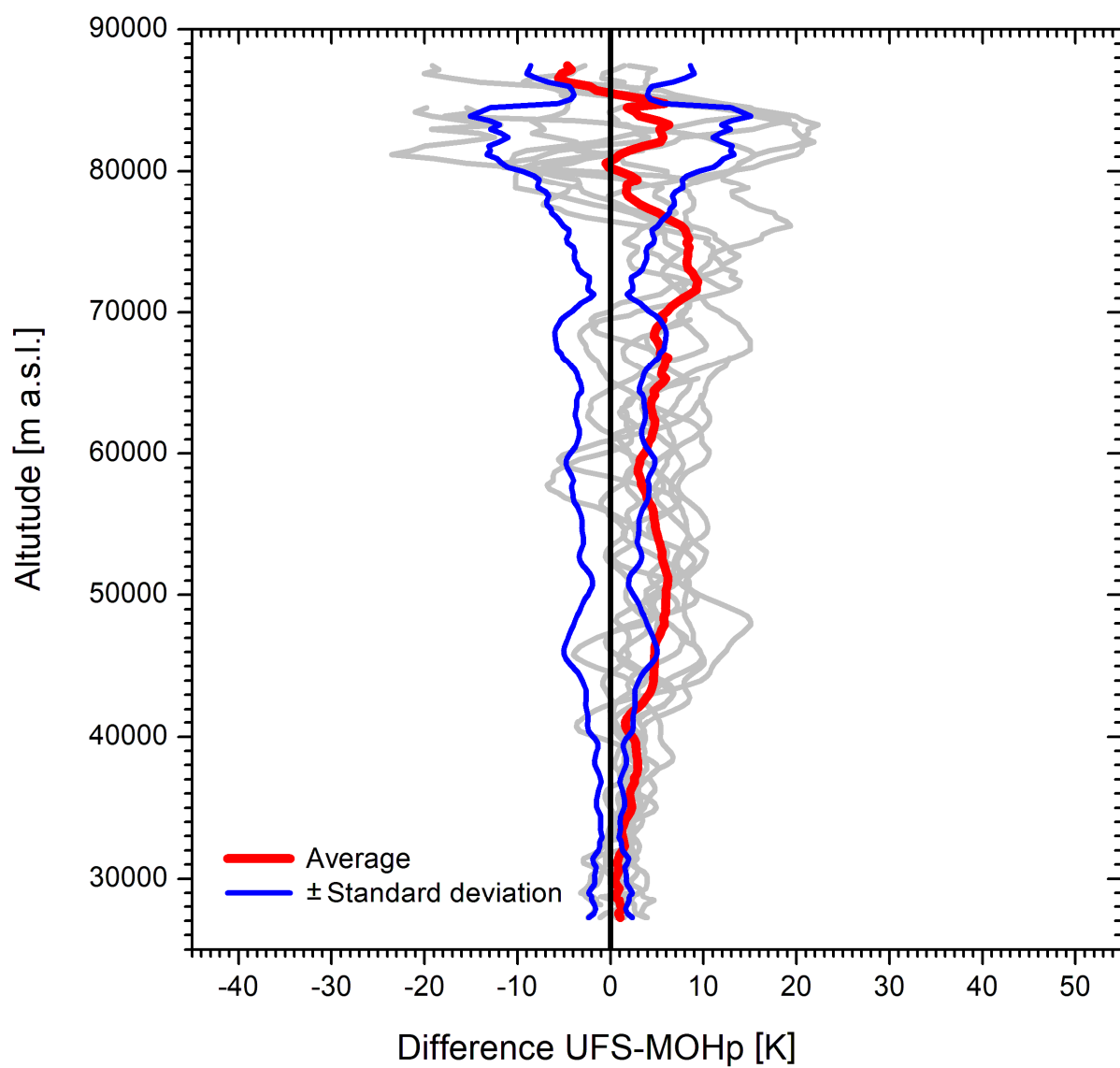
  Fig. 8. Differences of the 9 of the 14 temperature profiles of the UFS lidar with those of the MOHp lidar during

  the same night, together with their averages (red line) and positive and negative standard deviations (blue lines).

953
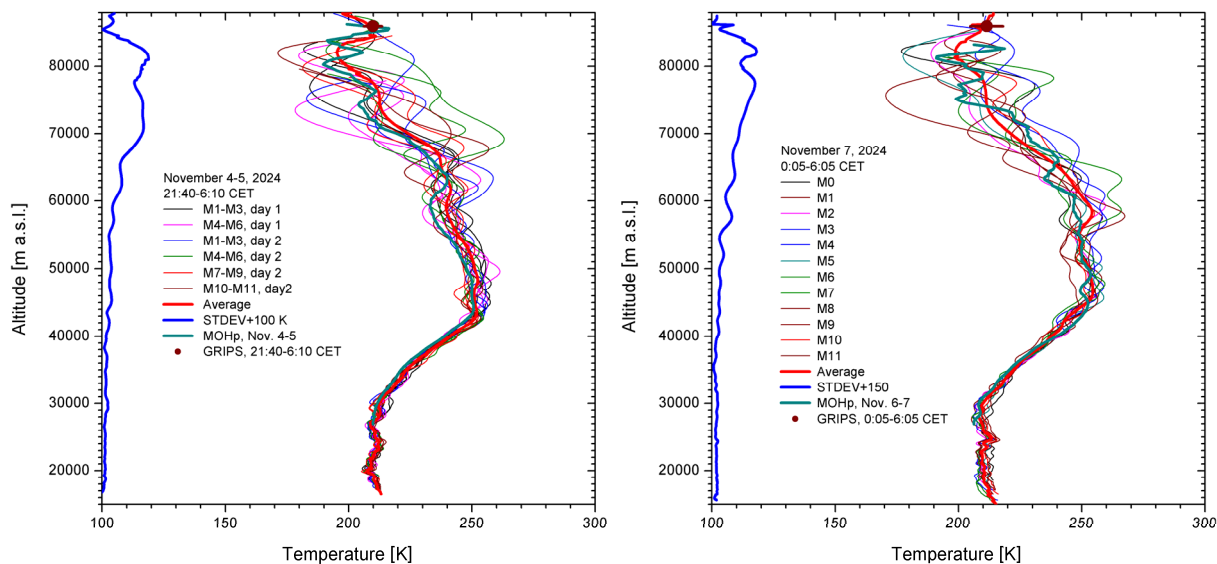
954 **Fig. 9**. Two of the four night-time series of the UFS 0.5-h temperature profiles in November 2024, compared
955 with the all-night T profiles obtained at MOHp and the GRIPS average during the lidar measurement periods:
956 Left panel: 4 November 2024 (start at 21:40 CET) to 5 November 2014 (end at 6:10 CET, beginning of the
957 dawn); groups of three subsequent profiles (M means measurement) are presented share the same colour in order
958 to reduce confusion.
959 Right panel: 7 November 2014 (0:05 to 6:05 CET); all profiles for measurements 0 to 11 are coloured
960 differently, from black and violet to red.
961 The standard deviations (STDEV) are shown in blue after adding 100 K.

962

963

964
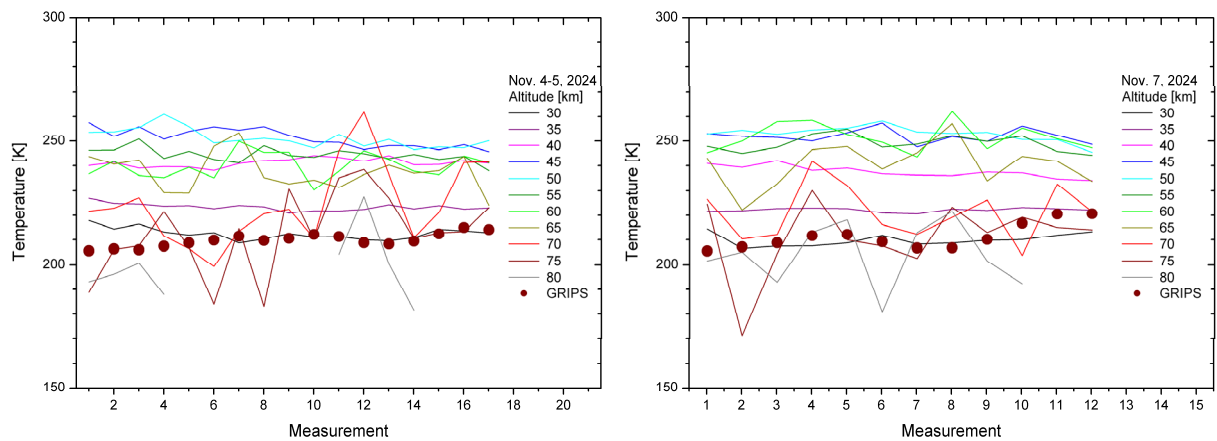
965 **Fig. 10**. Time series for the two examples shown in Fig. 8 for selected altitudes listed in the legend, together with
966 half-hour averages of the GRIPS temperatures; here, the measurements are labelled from the beginning to the
967 end of the night-time series.

968

969

970

971
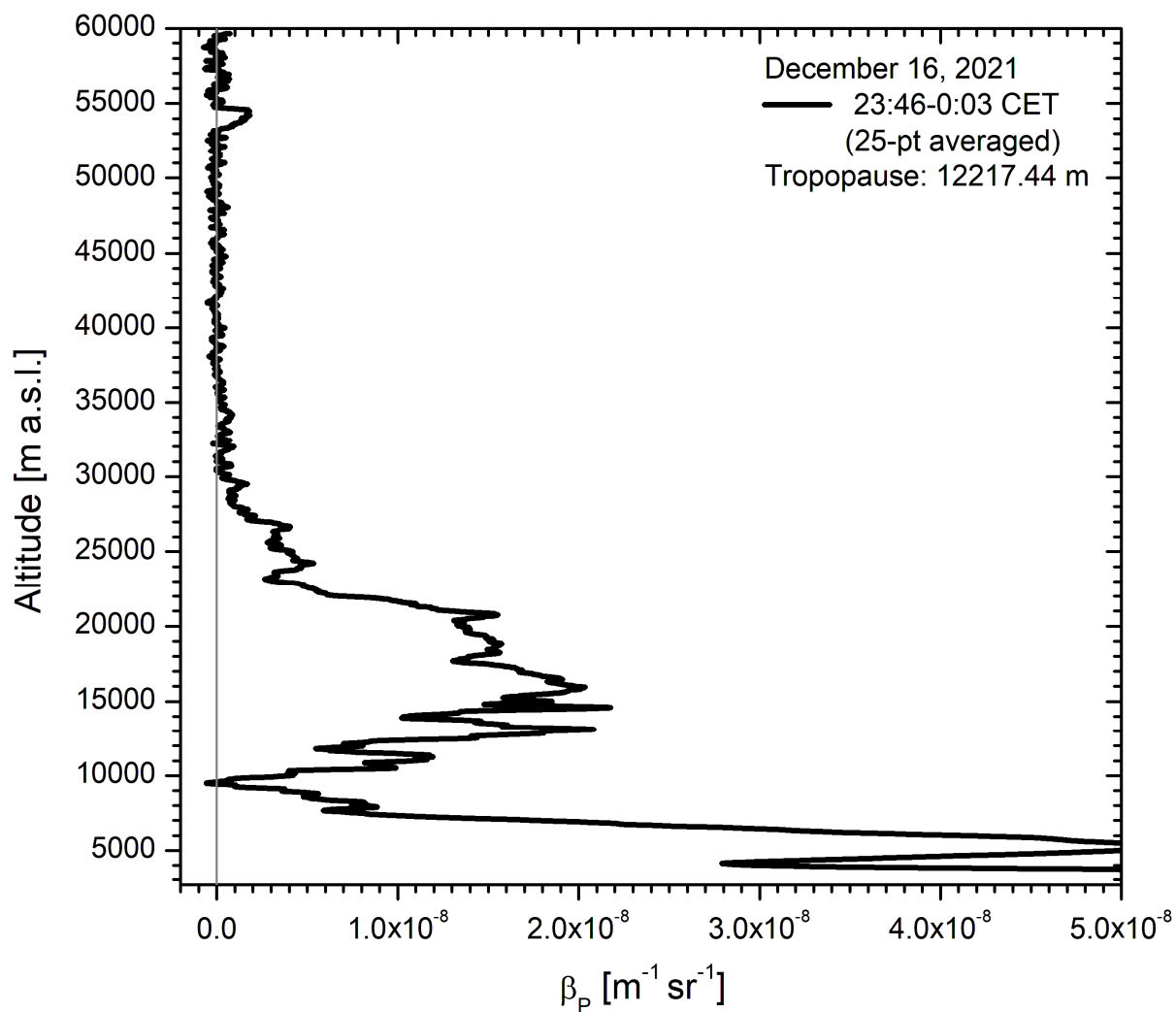
972   **Fig. 11**. 532.2-nm aerosol backscatter coefficients β_P from a night-time measurement with the UFS stratospheric

973   aerosol lidar showing a strange peak at 54 km.

974

975